3D test simulations of the outer radiation belt electron dynamics including electron-chorus resonant interactions

Athina Varotsou [1], Daniel Boscher [2], Sebastien Bourdarie [2], Richard B. Horne [3], Nigel P. Meredith [3], Sarah A. Glauert [3], Reiner H. Friedel [1]

(1) Space Science and Applications, Los Alamos National Laboratory,

Los Alamos, NM, USA,

(2) Office National d'Etudes et Recherches Aérospatiales, Toulouse, France,

(3) British Antarctic Survey, Natural Environment Research Council, Cambridge, UK

athina@lanl.gov, daniel.boscher@oncert.fr, sebastien.bourdarie@onecert.fr, RH@bas.ac.uk,

nmer@bas.ac.uk, sagl@bas.ac.uk, friedel@lanl.gov

14 **Abstract**

15   We present results from our 3D simulations using the Salammbô electron radiation belt

16 physical model. We have run steady state and dynamic storm test-case simulations to

17 study the effect of electron-chorus resonant interactions on the radiation belt electron

18 dynamics. When electron-chorus interactions are introduced in the code outside the

19 plasmasphere, results show that a seed population with a kappa distribution and a

20 characteristic energy of 2 keV is accelerated up to a few MeV in the outer radiation belt.

21 MeV electron fluxes increase by an order of magnitude during high magnetic activity

22 conditions especially near L^*~5 and for equatorial mirroring particles. We have also

23 performed a parametric study of various important parameters to investigate how our

24 results could be influenced by the uncertainty that characterizes their values. Results of

25 this study show that if we consider higher values of the radial diffusion coefficients,

26 different initial states and different boundary conditions, we always observe a peak in the

27 L*-profile of the MeV electrons when electron-chorus interactions are included.

1. Introduction

Since the discovery of the radiation belts in 1958 [*Van Allen et al.*, 1958], a lot of progress has been made in understanding and describing the Earth's radiation environment. Scientific and operational satellite data combined with physical simulations have provided a great insight into the dynamics of the charged particle population and the physical processes involved.

One of the most important remaining questions is the definition of the physical processes responsible for the loss and acceleration of relativistic radiation belt electrons. During conditions of high geomagnetic activity these processes are enhanced causing the observed high variability of high energy electrons especially in the outer radiation belt. Relativistic electron fluxes will decrease if losses dominate, but if sources dominate, relativistic electron fluxes will increase, as is observed in approximately half of all moderate and intense geomagnetic storms [*Reeves at al.*, 2003]. The electron variation can be of several orders of magnitude on timescales from hours to days.

Several processes have been proposed to be responsible for the electron energization to MeV energies [e.g., *Friedel et al.*, 2002; *Horne*, 2002]. Radial diffusion was identified from the beginning as one of the most important [*Falthammar*, 1965, 1966]. Charged particles are transported inwards (towards the Earth) across magnetic field lines due to magnetic and electric field variations. Due to the conservation of the first adiabatic invariant (the particle's magnetic moment) particles moving towards regions of stronger magnetic field become more energetic. For equatorial particles the relationship between the energy of the particle and L- the distance (in Earth radii) of a magnetic field line from the center of the Earth at the equator [*McIlwain*, 1961]- is given by:

51

$$E_1\left(E_1 + 2E_0\right) * L_1{}^3 = E_2\left(E_2 + 2E_0\right) * L_2{}^3 \qquad (1)$$

53

where E_1 and L_1 are the initial energy and distance (from the center of the Earth, in Earth radii) of the particle and E_2 and L_2 are the final energy and distance of the particle. E_0 is the rest energy of the electron which is equal to 0.511 MeV. In addition, enhanced ULF wave activity in the outer electron radiation belt has been associated with enhanced radial diffusion during high magnetic activity conditions [*O'Brien et al.*, 2001; *Elkington et al.*, 1999].

However, numerous recent studies have shown that radial diffusion alone cannot explain all the temporal and spatial flux variations observed [*Reeves et al.*, 1998; *Brautigam and Albert*, 2000; *Obara et al.*, 2000; *Miyoshi et al.*, 2003; *Horne et al.*, 2003b; *Green and Kivelson*, 2004; *Horne et al.*, 2005; *Chen et al.*, 2006; *Fox et al.*, 2006; *Iles et al.*, 2006; *Miyoshi et al.*, 2006; *Shprits et al.*, 2006c; *Chen et al.*, 2007]. *Brautigam and Albert* [2000] studied the October 9, 1991 storm using CRRES data. When they tried to reproduce the measured fluxes with a simple radial diffusion physical model their results underestimated relativistic electron fluxes around L = 4-4.5 and the flux increase during the recovery phase was not well represented by the model. From the data analysis they also observed outward radial diffusion from L = 4-5 during the recovery phase. The same storm was selected by *Horne et al.* [2003b] who studied the electron pitch angle distribution and found it to be energy dependent.

Miyoshi et al. [2006] used the 4D relativistic RAM electron model [*Jordanova et al.*, 1996, 2003; *Jordanova and Miyoshi*, 2005] to simulate the energetic electron dynamics

74   during the October 2001 storm. Their results showed that radial diffusion, the only

75   mechanism included in the model for relativistic energies (E>300 keV), was not

76   sufficient to reproduce the observations. They concluded that an additional mechanism is

77   needed to explain high energy electron enhancements during the storm's recovery phase.

78   *Reeves et al.* [1998], studied the global response of relativistic radiation belt electrons

79   to the January 1997 magnetic cloud using data from LANL geosynchronous, GOES,

80   GPS, POLAR, SAMPEX and HEO and showed that fluxes increased first near $L = 4$ and

81   then at geosynchronous orbit, at $L = 6.6$.

82   *Green and Kivelson* [2004] in their study using POLAR data showed phase space

83   density expressed data as a function of $L*$ and time for off-equatorial MeV electrons

84   where a local peak appears near $L* = 4$-5 during the recovery phase. Similar phase space

85   density profiles were found by *Chen et al.* [2006, 2007] at the equator from combining

86   POLAR, LANL geosynchronous and GPS data. Developing peaks in the electron phase

87   space density were also found in the region $4 < L* < 5.5$ during relativistic electron flux

88   enhancements observed by the CRRES satellite [*Iles et al.*, 2006].

89   All the above results indicate that radial diffusion is not the only mechanism acting on

90   radiation belt electrons in the outer belt and that a local source is acting which dominates

91   other processes in the $L = 4$-5 region.

92   Many theoretical, observational and modeling studies have shown that the most

93   probable mechanism acting locally as a high energy electron source is the resonant

94   interaction of electrons with whistler-mode chorus waves leading to energy diffusion of

95   lower energy particles to higher energy. The in situ wave-particle heating mechanism was

96   theoretically discussed decades ago [*Kennel and Engelmann*, 1966; *Kennel*, 1969; *Lyons*,

97   1974] and agrees well with the scenario first proposed by *Thorne et al.* [1974] of

98   important energy diffusion occurring outside the plasmasphere during active geomagnetic

99   times when whistler-mode waves are present. More recently, *Horne and Thorne* [1998]

100   studied different types of electromagnetic waves present in the magnetosphere to estimate

101   the effect these waves could have on the trapped electron population. Whistler-mode

102   waves in the low density environment outside the plasmasphere were found to be good

103   candidates for electron acceleration to MeV energies from in situ energy diffusion of

104   lower energy particles. Following theoretical studies also demonstrated that cyclotron and

105   Landau resonances with whistler-mode chorus waves were the most probable mechanism

106   to produce local acceleration to MeV energies [*Summers et al.*, 1998; *Horne et al.*, 2003a;

107   *Glauert and Horne*, 2005].

108   Observational evidence for chorus-driven electron acceleration to relativistic energies

109   has been mostly provided by CRRES data studies where both particle and plasma wave

110   data were provided [*Meredith et al.*, 2002a,b, 2003a]. *Meredith et al.* [2003a] studied 26

111   geomagnetically disturbed periods and clearly showed the correlation between high levels

112   of lower-band chorus activity and relativistic electron enhancements in the outer radiation

113   belt. Similar studies are currently being performed using POLAR particle and wave data

114   [*Kristine Sigsbee*, GEM 2007 poster and personal communication].

115   Apart from theoretical and observational evidence for chorus-driven electron

116   acceleration to MeV energies, recent radiation belt 2D and 3D modeling efforts have

117   focused on this topic also. *Varotsou et al.* [2005] presented the first results from 3D

118   simulations with the Salammbô physical model [*Beutier and Boscher*, 1995; *Bourdarie et*

119   *al.*, 1996] including both radial diffusion and energy diffusion due to electron-chorus

resonant interactions. The simulations showed that when electron-chorus resonant interactions are included in the simulation, an initial seed population of electrons with characteristic plasmasheet energy of 5 keV can be locally accelerated to MeV energies in the outer belt near geosynchronous orbit.

In a two dimensional study by *Albert and Young* [2005] the diffusion equation was solved for energy and pitch angle diffusion due to chorus waves including the cross diffusion terms. The authors found that at $L = 4.5$ phase space density was strongly diffusing from 0.2 MeV up to a few MeV in less than a day.

Recently, *Li et al.* (2007) used the 2D UCLA radiation belt model, including energy and pitch-angle diffusion at a fixed L value and showed that the net effect of electron-chorus resonant interactions- including both dayside and night side parallel propagating chorus- is the local acceleration of relativistic electrons. The local increase of MeV fluxes during the recovery phase of a simulated storm persisted even after they introduced strong losses due to EMIC waves and plasmaspheric hiss.

In this paper we present a more detailed study that follows the first results presented by *Varotsou et al.* [2005]. We use the 3D Salammbô code to test the effect of each process (loss, acceleration, diffusion) on the flux and phase space density (PSD) profiles of relativistic electrons. The goal of our study is to investigate how different physical processes acting on the electrons influence the radiation belt dynamics. The study is performed for idealistic dynamic test-cases by using a physical model. The advantage of using a physical model is that we can 'turn on' or 'turn off' one of these processes to identify its effect on the radiation belt dynamics. We are not trying to reproduce satellite observations during a storm period at this point. More realistic simulations, using the

143 actual *Kp* variation and a boundary condition from geosynchronous measurements and

144 including high latitude chorus and EMIC waves, are being performed and will be

145 presented in a following paper.

146   The outline of the paper is as follows. The Salammbô 3D model for radiation belt

147 electrons is described in Section 2 and in Section 3 the diffusion coefficients for the

148 electron-chorus interactions are presented together with the method we followed to

149 introduce them into the code. The steady state and dynamic simulations are presented in

150 Section 4, followed by a parametric study for several key parameters in Section 5. In

151 Section 6 we discuss the limitations of the present study and our future goals, and in

152 Section 7 we summarize the results and conclusions of our study.

153

154 **2. The Salammbô 3D electron model**

155   The development of the Salammbô 3D code for the Earth's radiation belts started in the

156 1990s at ONERA in Toulouse, France and continues until today [*Beutier and Boscher*,

157 1995; *Beutier et al.*, 1995; *Bourdarie et al.*, 1996; *Vacaresse et al.*, 1999; *Varotsou et al.*,

158 2005; *Maget et al.*, 2007]. There are two versions of the code, one for protons and one for

159 electrons since the physical processes involved are different in each case. *Beutier and*

160 *Boscher* [1995] first presented the electron physical model based on a Fokker-Planck

161 diffusion equation solved in the (M,J,L^*) phase space, where M is the first adiabatic

162 invariant, the particle's magnetic moment, J is the second adiabatic invariant related to

163 the particle's bounce motion and L^* is the Roederer parameter [*Roederer*, 1970], related

164 to the third adiabatic invariant Φ by $\Phi = 2\pi\alpha^2 B_0/L^*$ (where α is the Earth's mean

165 radius and B_0 is the equatorial magnetic field magnitude at the Earth's surface). Physical

166 processes included were: radial diffusion, frictional processes by Coulomb interactions

167 with plasmaspheric cold electrons, pitch angle diffusion by Coulomb interactions with

168 atoms and molecules of the high atmosphere and pitch angle diffusion by wave-particle

169 resonant interactions inside the plasmasphere. This version of the code was used by

170 *Bourdarie et al.* [1996] in their effort to simulate the dynamics of radiation belt electrons

171 during a magnetic storm.

172 The current version of the Salammbô 3D code solves the Fokker-Planck equation to

173 estimate electron PSD in the (E, y, L^*) space, where E is the particle's kinetic energy, y is

174 the sine of the particle's equatorial pitch angle, α_{eq}, and L^* is the Roederer parameter. The

175 diffusion equation then translates to the following

176

177
$$\frac{\partial f}{\partial t} = L^{*2} \frac{\partial}{\partial L^*}\left(\frac{D_{LL}}{L^{*2}} \frac{\partial f}{\partial L^*} \right) + \frac{1}{yT(y)} \frac{\partial}{\partial y}\left(yT(y)D_{yy} \frac{\partial f}{\partial y} \right) + \frac{1}{a} \frac{\partial}{\partial E}\left(aD_{EE} \frac{\partial f}{\partial E} \right)$$

178
$$-\frac{1}{a} \frac{\partial}{\partial E}\left(a \frac{dE}{dt} f \right) \tag{2}$$

179

180 where the terms on the right hand side express radial diffusion, pitch angle diffusion

181 (where $T(y)$ is an auxiliary function occurring in the bounce frequency expression),

182 energy diffusion (where $a = (E + E_0)[E(E + 2E_0)]^{1/2}$, E_0 the electron rest energy) and

183 losses due to friction, respectively. Radial diffusion is assumed under constant first and

184 second adiabatic invariants on one grid. Pitch angle diffusion occurs under constant

185 energy and L^* and energy diffusion is considered under constant pitch-angle and L^* on a

186 second grid. Interpolation methods are used between the two grids. We use logarithmic

187 grids in energy and L^* and a uniform grid in pitch angle. No cross diffusion terms are

188   included in the current version of the code. The introduction of cross diffusion terms is a

189   difficult task which is under study and development [*Albert and Young*, 2005]. The

190   magnetic field used in Salammbô is a dipolar, tilted and eccentric field.

191   The physical processes that drive radial, pitch angle and energy diffusion in the

192   Salammbô code are described in Table 1 (see also diagram in Figure 1 of *Maget et al.*,

193   2007). The fourth and fifth columns indicate which calculation and which parameters

194   were used for the definition of the diffusion coefficients. Note here that radial diffusion

195   coefficients are different from the ones used by *Varotsou et al.* [2005].

196   Inside the plasmasphere, particles interact with hiss, VLF transmitters and lightning-

197   generated whistlers. Outside the plasmasphere, particles interact with whistler-mode

198   chorus waves. In this paper we mainly focus on the region outside the plasmapause where

199   both radial diffusion and chorus waves occur (for more details on the plasmasphere and

200   inner belt region refer to *Beutier and Boscher* [1995]).

201   In addition to these diffusive processes, particle energy loss by Coulomb interactions

202   with cold plasmaspheric electrons and bound electrons of atoms and molecules of the

203   high atmosphere are considered. This process is expressed by the frictional term in the

204   diffusion equation (2). However, interactions with the high atmosphere don't have a

205   significant effect on outer radiation belt electron dynamics, so we will not be analyzing

206   this physical process in any detail (for more details see *Beutier and Boscher* [1995]).

207   In the code, the temporal evolution of PSD is determined by the temporal evolution of

208   the coefficients introduced in the diffusion equation (2). Radial diffusion coefficients and

209   pitch angle and energy diffusion coefficients due to chorus interactions outside the

210   plasmasphere are expressed as a function of geomagnetic activity through the *Kp* index

211   which is time dependent. Furthermore, the position of the plasmapause, which separates

212   the regions where plasmaspheric waves and chorus operate, is also Kp dependent

213   [*Carpenter and Park*, 1973]. The intensity of plasmaspheric waves is considered to be

214   constant (not activity dependent) in Salammbô (see Discussion section). The expressions

215   used for the diffusion coefficients together with the boundary conditions and our solving

216   scheme of equation (2) will be described in the following Sections.

217

218   **3. Electron – chorus resonant interactions**

219   **3.1 Diffusion coefficients from PADIE**

220   Pitch angle, D_{yy}, and energy diffusion, D_{EE}, coefficients for cyclotron resonant electron

221   - chorus interactions have been estimated from the PADIE code [*Glauert and Horne*,

222   2005]. The calculation is done using the quasi-linear assumption and is fully relativistic.

223   In the calculation, distributions of wave power and wave normal angles are assumed to

224   be Gaussian [e.g. *Lyons*, 1974]. The wave distribution is considered to peak along the

225   magnetic field direction with an angular spread of 30 degrees. Landau and $\pm$ 5 cyclotron

226   harmonic resonances are included in the calculation and waves are assumed to be

227   confined near the equator at magnetic latitudes of $-15^0 < \lambda_m < 15^0$. The conditions and

228   parameters used for the calculation are the same as those used by *Varotsou et al.* [2005],

229   presented here in Table 2. These values are based on wave observations from the Plasma

230   Wave Experiment [*Anderson et al.*, 1992] on board the CRRES spacecraft [*Glauert and*

231   *Horne*, 2005].

232   Bounce averaged diffusion coefficients D_{yy} and D_{EE} are calculated by the PADIE code

233   as a matrix with a constant wave amplitude of B_w = 100nT for electron plasma frequency

234 to electron cyclotron frequency ratio (*fpe/fce*) values of 1.5, 2.5, 5.0, 7.5 and 10, electron

235 energies of 0.01, 0.03, 0.1, 0.3, 1, and 3 MeV, and *L* values of 2.5, 3.5, 4.5, 5.5 and 6.5,

236 with a resolution of less than 1 degree equatorial pitch angle. Diffusion coefficients are

237 set to zero for energies $E < 0.01$ MeV and $E > 3$ MeV and for *L* values $L < 2.5$ and $L >$

238 6.5. For *fpe/fce* < 1.5 and *fpe/fce* > 10 diffusion coefficients are assumed constant and

239 equal to their values for *fpe/fce* = 1.5 and *fpe/fce* = 10, respectively.

240

241 **3.2 Introduction of D_{yy}, D_{EE} in Salammbô**

242   The diffusion coefficients were related to magnetic activity by constructing a statistical

243 wave model where equatorial values ($-15^0 < \lambda_m < 15^0$) of *f*pe/*f*ce and wave intensity B_{wave}^2

244 measured by CRRES were parameterized for $Kp < 2$, $2 \leq Kp \leq 4$ and $Kp \geq 4$ between $L =$

245 1 to 7, with a resolution of 0.1*L* and 1 hour in *MLT* [*Meredith et al.*, 2003b]. The

246 coefficient values from the matrix given by PADIE were interpolated to energy, pitch

247 angle and *L* values corresponding to the Salammbô grid and to *fpe/fce* values

248 corresponding to the ones given from the statistical wave model (CRRES data).

249   For a given energy, *L*, pitch angle and *Kp*, the diffusion coefficients were calculated in

250 each *MLT* bin according to *fpe/fce* and B_{wave}^2. Finally, for introduction in the Salammbô

251 code, we calculated the coefficients' drift average by summing values over all MLT and

252 dividing by the number of MLT bins. Since electron-chorus interactions are most

253 efficient for low *fpe/fce* and high wave intensities [*Meredith et al.*, 2003b], they were

254 only included in the model outside the plasmasphere.

255   An example of the bounce and drift averaged diffusion coefficients is presented in

256 Figure 1 for $L^* = 4.8$. The first column shows the energy diffusion coefficients as a

257   function of energy and equatorial pitch angle for the three different Kp categories and the

258   second column shows the same dependence for the pitch angle diffusion coefficients.

259   Some important conclusions can be drawn from Figure 1: a) both coefficients increase

260   when geomagnetic activity (Kp) increases, b) for high energies both coefficients obtain

261   higher values at higher pitch angles, thus acceleration will be more important near the

262   equator and no high energy electron losses due to diffusion in the loss cone (low

263   equatorial pitch angle values) by chorus waves will occur, and c) pitch angle diffusion for

264   the low energy particles near the loss cone will be fast, thus these particles will

265   experience important losses due to the interaction with chorus waves.

266

267   **4. Test-case simulations**

268   We solve the diffusion equation (2), using an explicit finite difference scheme, in the E, y

269   ($=\sin\alpha_{eq}$), L^* space in a rectangular domain with 25 nodes in each direction (we chose the

270   number of nodes for a fast execution since the time step of our calculations is limited by

271   the Courant-Friedrichs-Lewy condition [*Courant et al.*, 1967]). The simulation domain in

272   Salammbô extends for energies from 0.1 keV to 5 MeV, pitch angles from 2 degrees to

273   90 degrees (the lower limit for the equatorial pitch angle, under which electrons are lost

274   in the upper atmosphere, is calculated in the model for each L^* shell- it doesn't take

275   values of less than 2^0) and L^* shells from 1 to 8. Since electron-chorus interactions are

276   introduced in the code for energies from 10 keV to 3 MeV and L* values from outside the

277   plasmapause to 6.5 and since our goal is to test if these interactions can lead to electron

278   acceleration to MeV energies, the domain of interest in this study, on which we will

279   focus, is for $E > 0.5$ MeV and L* > 3.

280   The boundary conditions we impose for the solution of the diffusion equation are the

281   following

282

283             $f(E_{\min}) = f_{bound}(E_{\min})$ $f(E_{\max}) = 0$

284                 $f(\alpha_{eq\,\min}) = 0$ $f(\alpha_{eq\,\max}) = \partial f / \partial \alpha = 0$

285                 $f(L^*{}_{\min}) = 0$ $f(L^*{}_{\max}) = f_{bound}(E)$

286

287   where f_{bound} is the outer boundary condition (only a function of electron energy) we

288   impose at $L^* = 8$, which constitutes the source of electrons in the simulation. In our

289   current study this condition is constant with time (a time varying boundary is currently

290   being studied and will be presented in a future paper). With the above boundary

291   conditions we consider that: a) the lowest energy PSD- at the outer boundary- stays

292   constant and there is an absence of multi-MeV energies, b) the loss cone is empty and the

293   pitch angle particle distribution at the equator is flat, and c) losses dominate at $L^* = 1$ and

294   the source at $L^* = 8$ is constant and given by the f_{bound} boundary condition.

295   The boundary condition at $L^* = 8$ is defined to be a kappa distribution [*Christon et al.*,

296   1991] given by the formula

297

298                  $$f_{bound} = A\left[1 + \frac{E}{kE_0}\right]^{-k-1}$$ (3)

299

300   where we take $A = 10^{35}$ MeV^{-3}s^{-3}, defined by examining a long period of LANL

301   geosynchronous measurements, $E_0 = 2$ keV (plasmasheet characteristic energy) , defined

14

302   by average LANL geosynchronous MPA (Magnetospheric Plasma Analyzer) data

303   [*Joseph Borovsky* private communication 2007] and $k = 5$, based on *Christon et al.* [1988,

304   1991]. Note here that *Varotsou et al.* [2005] used a kappa distribution with a

305   characteristic energy of 5 keV, considering a higher energy spectrum at the source.

306   Finally, to help the reader follow the work and results presented in the following

307   Sections we summarize in Table 3 the physical processes involved in radiation belt

308   dynamics outside the plasmasphere in Salammbô, together with the expressions of the

309   coefficients introduced in the diffusion equation (2) and the simulation domain where

310   each process is included. The plasmapause position is defined by the empirical

311   expression $Lpp = 5.6 - 0.46Kp'$ [*Carpenter and Park*, 1973], where Kp' is the highest

312   value of the Kp index during the last 24 hours of the simulation.

313

314   **4.1. Steady state**

315   First we present the results obtained for a steady state of the radiation belts. There is no

316   dynamics and no time dependence involved here. This permits us to detect the effect

317   electron-chorus interactions have on the radiation belt electrons when we include them in

318   our simulation scheme. In addition, the initial state for the dynamic simulation is defined

319   from the output of this steady state simulation.

320   In the steady-state simulation, the diffusion equation (2) is solved for $\partial f/\partial t = 0$. The

321   steady state is defined for a certain geomagnetic activity level, i.e., for a given Kp value.

322   When we fix Kp to a constant value, radial diffusion coefficients depend only on L^*,

323   while pitch angle and energy diffusion coefficients depend on energy, pitch angle and L^*,

324   and the plasmapause is fixed to a certain L^* shell.

325   Radiation belts are considered to initially be empty everywhere except at the outer

326   boundary ($L^* = 8$) where the source is defined by equation (3). After many iterations, the

327   system reaches a steady state and the calculated phase space densities represent the state

328   of the radiation belts after a long period of steady conditions.

329   We run the code for $Kp = 1.3$ to use the output as an initial state of calm conditions for

330   our dynamic simulation. To investigate the effect of electron-chorus resonant interactions

331   on the electron distribution we performed one simulation including this process and one

332   without it. The results are presented in Figures 2, 3 and 5.

333

334   **4.1.1. PSD variation as a function of L shell**

335   In Figure 2, phase space densities are presented as a function of L^* shell and iteration

336   number for a constant magnetic moment value of $M = 2100$ MeV/G and for equatorial

337   mirroring particles ($\alpha_{eq} = 90$ degrees). The plasmapause position is marked with a white

338   line.

339   In these type of plots, energy increases as we move inwards to lower L^* shells. For $M =$

340   2100 MeV/G, we are studying ~1 MeV electrons at $L^* \sim 6$ and ~2 MeV electrons at $L^* \sim$

341   4.5. We choose to represent results in a (M, α_{eq}) = constant space instead of a (M, J) =

342   constant space (where J is the second adiabatic invariant) because we want to be able to

343   distinguish between different processes affecting the electron distribution. In addition, α_{eq}

344   = constant is not that different from J = constant.

345   Figure 2(a) shows results when electron-chorus interactions are included in the

346   simulation together with radial diffusion. First, particles are transported inwards (in the

347   initially empty radiation belts) from the outer boundary by radial diffusion and then they

16

348   are accelerated by chorus waves resulting to the formation of a peak in the PSD

349   distribution at $L^* \sim$ 5-6. Then, phase space density at surrounding L^* shells (lower than 5

350   and higher than 6) increases due to radial diffusion diffusing particles away from the

351   peak. As a result, phase space density increases inside the plasmasphere and outside $L^* =$

352   6.5, regions where electron-chorus interactions are not considered in the simulation.

353   In contrast, in Figure 2(b), where results with only radial diffusion included in the

354   simulation are shown, there is no peak forming in the PSD distribution in L^* shell.

355   Particles are only diffused inwards forming a flat PSD distribution. The maximum

356   difference in the PSD values between the two steady states is observed at $L^* = 5.5$ and is

357   equal to two orders of magnitude. These kinds of increases have been observed at

358   geosynchronous and GPS orbits [*Chen et al.*, 2007].

359

360   **4.1.2. PSD variation as a function of equatorial pitch angle**

361   In Figure 3, results from the two simulations (with and without chorus waves) are

362   presented for comparison as a function of equatorial pitch angle for $L^* = 5.2$ and for $E =$

363   1.7 MeV. We choose to present results with respect to energy, equatorial pitch angle and

364   L^* values to confirm that introduction of electron-chorus interactions in a 3D particle

365   simulation leads to energy diffusion, i.e., acceleration of electrons to MeV energies.

366   When electron-chorus resonant interactions are introduced in the simulation we observe

367   an increase in the PSD level. This increase is greater for equatorial pitch angles of 50

368   degrees and higher. Flat top pitch angle distributions like this are a signature of chorus

369   wave acceleration and have been observed by the CRRES satellite (*Horne et al.*, 2003b).

370   The profile of the red curve (when chorus waves are included in the simulation) can be

371   explained if we look at the profile of the energy and pitch angle diffusion coefficients as a

372   function of equatorial pitch angle. Both coefficients are plotted in Figure 4 for the same

373   parameters as in Figure 3. Energy diffusion coefficients obtain maximum and almost

374   steady values for equatorial pitch angles between 60 and 90 degrees. For α_{eq} < 60

375   degrees, D_{EE} decreases very fast with decreasing pitch angle, becoming one order of

376   magnitude smaller every ~10 degrees. Pitch angle diffusion coefficients are higher in the

377   region of 50-70 degrees. Their role is to diffuse equatorial particles to lower pitch angle

378   values. Thus, PSD values increase for all equatorial pitch angles (red curve in Figure 3).

379   In general we conclude that the effect of introducing chorus waves in our simulations is

380   most important for equatorial particles, down to a value of α_{eq}~50 degrees. This is related

381   to our initial hypothesis that chorus waves are confined near the equator (see Discussion

382   section).

383

384   **4.1.3. PSD variation as a function of energy**

385   Finally, in Figure 5, results are presented as a function of energy for $L^* = 5.2$ and for

386   equatorial particles (α_{eq}=90 degrees). As in the previous figures, results from the

387   simulation with electron-chorus interactions (red curve) and without (blue curve) are

388   compared. When chorus waves are included, energy diffusion- by which lower energy

389   electrons are accelerated to higher energies- becomes very important. Higher energy

390   phase space densities increase significantly, while lower energy (less than 30 keV) phase

391   space densities decrease. As an example, 600 keV and 1.7 MeV electron phase space

18

392 densities increase by more than 2 orders of magnitude while ~ 20 keV electron PSD

393 becomes 2 times smaller.

394 In reality we don't see low energies decreasing while higher ones increase. The

395 decrease of the low energy phase space densities is an artifact of our simulations since we

396 are considering a constant outer source and convection is not included in the simulation.

397 Observations show that times of enhanced chorus activity coincide with times of

398 enhanced injections and substorm activity [*Meredith et al.*, 2001, 2002a, 2003a]. Thus,

399 the low energy source increases during these times.

400

401 **4.2 Dynamic simulation**

402 During high geomagnetic activity conditions, variations in the trapped electron

403 distribution can be important and in many cases very fast. Modeling these variations

404 requires a good understanding of the physical processes involved in radiation belt- and

405 magnetospheric- dynamics.

406 Here, the goal is to expand the study on the combined effect of radial diffusion and

407 electron-chorus resonant interactions presented by *Varotsou et al.* [2005]. We have

408 simulated a simple test-case where *Kp* varies step-wise from a low initial value to a

409 higher one and then back to the initial one. The *Kp* profile for this simulation is shown in

410 Figure 6. We chose *Kp* to be initially equal to 1.3 to simulate calm conditions. This initial

411 state is the steady state calculated in the previous section. Then, *Kp* becomes equal to 4

412 for one day and finally it returns to its initial low value. Next, we will focus on the

413 evolution of the electron distributions from time *T1* (initial state) to time *T2* (state after 1

414 day of *Kp* = 4) shown in Figure 6.

415

4.2.1. PSD as a function of L shell

When Kp increases, both radial diffusion and electron-chorus interactions are enhanced. To identify which process is responsible for the dynamics observed we perform three simulations: one where both radial diffusion and chorus interactions are included, one where we 'turn off' radial diffusion and one where we 'turn off' electron-chorus interactions. The initial state used is the same for all simulations. The results from the three simulations at time $T2$ are plotted in Figure 7. In this figure, phase space densities are plotted versus L^* shell for equatorial particles with magnetic moment equal to 2100 MeV/G. Also marked (vertical dashed lines) is the plasmapause position for $Kp = 1.3$ and $Kp = 4$.

When we 'turn off' radial diffusion, interactions with chorus waves are the only process acting on radiation belt electrons outside the plasmasphere. As a result, at time $T2$ phase space densities increase significantly creating a very pronounced peak at $L^* = 5.7$. This increase is confined in the region where chorus waves are defined in our simulation ($Lpp < L^* < 6.5$) and is maximal in the $L^* = 5-6$ region (increase of more than 2 orders of magnitude).

When we 'turn off' electron-chorus interactions, radial diffusion is the only process acting on electrons outside the plasmasphere. In this case, at time $T2$ phase space densities decrease at higher L^* shells ($L^* > 4.5$) and increase at lower L^* shells. This is the result of particles diffusing away from the peak that already exists in the initial state. During high activity conditions, enhanced outward radial diffusion from the peak- at $L^* \sim$ 5- towards higher L^* results in the decrease of PSD since particles are lost at the boundary

438   (which stays constant in our simulation). Inward radial diffusion is weaker, but we can

439   see a small increase in PSD at $L^* < 4.5$.

440   Finally, when both processes are included in the simulation, the localized effect of

441   chorus waves is diffused by radial diffusion to all L^* shells. The peak value decreases

442   while values around the peak increase. This increase is more important at higher L^* shells

443   where radial diffusion is stronger, resulting at an important increase of PSD in the region

444   where chorus waves are not considered in the simulation ($L^* > 6.5$) [*Varotsou et al.,*

445   *2005*]. However, the most important increase in the PSD-$L*$ distribution- more than an

446   order of magnitude- is observed near $L* = 5-6$ ($E = 1-2$ MeV).

447

448   **4.2.2. PSD as a function of equatorial pitch angle and energy**

449   In Figure 8, results from all three simulations ('turning off' chorus, 'turning off' radial

450   diffusion and including both processes) are plotted versus equatorial pitch angle at $L* =$

451   5.2 and for $E = 1.7$ MeV particles. At this $L*$ we position ourselves at the peak of the

452   PSD distribution as shown in Figure 7 (red line).

453   Results agree well with those presented in Figure 7. Radial diffusion, when acting

454   alone, diffuses particles away from the peak in the initial PSD-L^* distribution decreasing

455   PSD at the peak location. This process is equally strong at all equatorial pitch angles-

456   since the D_{LL} coefficients do not depend on α_{eq}- but its effect depends also on $\partial f/\partial L$ at

457   each α_{eq} value.

458   When chorus interactions is the only process acting, PSD increases by a factor of ~ 100

459   for $\alpha_{eq} > 40$ degrees. Energy and pitch angle diffusion are much weaker at low equatorial

460   pitch angles for MeV electrons (see Figure 1 and 4).

461   When both processes are taken into account, radial diffusion weakens the effect of

462   chorus waves for $\alpha_{eq} > 30$ degrees by diffusing particles away from the peak created by

463   chorus interactions. However it is obvious that chorus interactions dominate over radial

464   diffusion at $\alpha_{eq} > 30$ degrees and the overall result is a net increase of electron PSD (more

465   than an order of magnitude) for these pitch angle values outside the plasmasphere.

466   In Figure 9, PSD is plotted versus energy (from 0.5 to 5 MeV) and equatorial pitch

467   angle for $L^* = 5.2$ at times $T1$ and $T2$. Phase space densities have greatly increased at time

468    $T2$ at the MeV energy range for $\alpha_{eq} > 30$ degrees in agreement with the results presented

469   in Figure 8. However at lower pitch angle values no increase is observed for the MeV

470   particles. To understand this behavior better we plot in Figure 10 for $Kp = 4$, as a function

471   of energy, (a) pitch angle diffusion coefficients D_{yy} for $\alpha_{eq} = 85$ degrees (solid line) and

472    $\alpha_{eq} = 30$ degrees (dash dot line) and (b) energy diffusion coefficients D_{EE} for $\alpha_{eq} = 90$

473   degrees (solid line) and $\alpha_{eq} = 30$ degrees (dash dot line).

474   For $\alpha_{eq} = 70\text{-}90$ degrees we do not expect pitch angle diffusion to play an important

475   role, since, as it is noted in Section 4.1, the initial pitch angle distribution at $T1$ is flat near

476   these values. In this region, energy diffusion is principally responsible for the dynamics

477   observed especially at higher energies as can be seen in Figure 10(b) for $\alpha_{eq} = 90$ degrees.

478   At $\alpha_{eq} = 30$ degrees the coefficient's values are very different from those at 90 degrees.

479   Figure 10(b) shows that energy diffusion coefficients for high energy electrons become

480   10^3 times weaker (even more in some cases). As a result, the increase of high energy

481   phase space densities in Figure 9 is much weaker at $\alpha_{eq} \sim 30$ degrees than at higher ones.

482

483   **4.2.3. Fluxes**

22

484   Since PSD is not a physical quantity that is measured by satellites, we show here our

485   results for the dynamic test-case simulation including both radial diffusion and electron-

486   chorus interactions as fluxes. In Figure 11, omnidirectional fluxes at the equator are

487   shown in an L^*-time space for 1.6 MeV. The plasmapause location is shown with a green

488   line and the Kp variation with time is shown on the top of the figure.

489   Once again we clearly observe the electron acceleration due to chorus interactions:

490   MeV fluxes increase in the heart of the radiation belts when activity increases. After 1

491   day of Kp = 4 fluxes become 24 times higher at L^* = 5.7 and 15 times higher at L = 6.6.

492   When Kp recovers to its initial low value, MeV fluxes keep increasing at L^* > 6 due to

493   radial diffusion. After the plasmapause relaxes to its initial position MeV fluxes inside

494   the plasmasphere decrease slowly.

495

496   **5. Parametric study**

497   In Sections 3 and 4 we presented the results of simulations including chorus

498   interactions in the Salammbô 3D code. The results showed clearly that a low energy seed

499   population can be locally accelerated by chorus waves to MeV energies in the heart of the

500   radiation belts near L^* = 5. However, many of the parameters used in the simulations are

501   quite uncertain, thus it is important to perform a parametric study where the sensitivity of

502   the results to the parameter's values can be quantified. Here we examine how results

503   change if we consider different values for three of the important parameters: 1) radial

504   diffusion coefficients, 2) initial state condition and 3) source condition at L^* = 8.

505

506   **5.1. Radial diffusion coefficients**

507   The accurate definition of radial diffusion coefficients constitutes one of the most

508   important projects in radiation belt physics. Although many efforts have been made to

509   calculate them empirically [*Lanzerotti et al.*, 1970; *Lanzerotti and Morgan*, 1973;

510   *Holzworth and Mozer*, 1979; *Brautigam and Albert*, 2000; *Li*, 2004] and theoretically

511   [*Falthammar*, 1965, 1966; *Schulz and Lanzerotti*, 1974; *Brizard and Chan,* 2001; *Perry*

512   *et al.*, 2005], there is still a lot of uncertainty concerning their dependence in L, energy,

513   pitch angle and magnetic activity.

514   As noted in previous sections, the result of the simulation performed using both radial

515   diffusion and chorus interactions depends on the relative intensity of the two processes. If

516   radial diffusion coefficients had lower values than the ones used here [*Brautigam and*

517   *Albert*, 2000] then the effect of chorus waves on the electron distribution would be even

518   more important. Here we examine how results change if we consider higher radial

519   diffusion coefficient values.

520   To investigate the influence of the radial diffusion coefficient's uncertainty on our

521   results we perform two simulations, increasing D_{LL} by a factor of three and six,

522   respectively. The results of both simulations for the steady case are plotted in Figure

523   12(a), together with the previous result- with the nominal *Brautigam and Albert* [2000]

524   coefficient values. The steady case simulation is for $Kp = 1.3$ and for $M = 2100$ MeV/G

525   equatorial particles. The number of iterations used is the same for all simulations.

526   Figure 12(a) shows that there is an important difference between the results of the three

527   simulations. When higher values are used for the radial diffusion coefficients, PSD

528   profiles become much more flat, or completely flat for the case where D_{LL} is increased by

529   a factor of 6. Radial diffusion erases almost completely the effect of chorus wave

530   interactions by diffusing particles away from the peak that tends to be created.

531   In Figure 12(b), results from the dynamic simulations are plotted versus L^* for 2100

532   MeV/G equatorial electrons. The dynamic simulation performed here is the same

533   dynamic test-case simulation as the one presented in Section 4.2: starting from an initial

534   low activity state (steady state for Kp = 1.3) we calculate the state of the electron

535   radiation belts after 1 day of high magnetic activity (1 day of Kp = 4). For the simulations

536   presented here, the common initial state used is a flat PSD distribution which corresponds

537   to the steady state calculated by using six times higher D_{LL} values.

538   Results after one day of Kp = 4 (time $T2$) are presented for the three different D_{LL}

539   values. The first thing that we notice is that even when an initial flat distribution is used,

540   irrespective of the size of D_{LL} used, the effect of chorus waves is easily distinguishable:

541   electrons are locally accelerated to MeV energies and a peak forms near L^* = 5.

542   The differences between the three curves at time $T2$ are at the location of the peak and

543   at the level of PSD. When higher D_{LL} values are used, the peak is less pronounced, moves

544   inwards in L^* and is characterized by lower PSD values. In these cases radial diffusion is

545   more effective in diffusing particles away from the peak that chorus interactions tend to

546   create. In addition, strong outward radial diffusion is more effective at high L^* values,

547   thus the peak of the electron distribution is now observed at lower L^* shells.

548

549   **5.2. Initial state condition**

550   We compare the dynamics resulting after 1 day of Kp = 4 for two different initial state

551   conditions as shown in Figure 13. State 1 has a flat L^*-profile and State 2 has a 'peaked'

552   L^*-profile with higher PSD values. From the comparison between dynamic state 1 (Dyn

553   1) and dynamic state 2 (Dyn 2) we conclude that phase space densities increase much

554   faster in the case where the flat, lower initial state is used, reaching peak values similar to

555   the ones for the case where the higher peaked initial state is used. The two initial states

556   are different by a factor of ~115 at the peak location ($L^* = 5.2$), however the two dynamic

557   states are different by only a factor of ~ 6.

558   The reason for this difference is the fact that radial diffusion will initially be much

559   weaker in the simulation using State 1, since $\partial f / \partial L = 0$ for all L^* values greater than $L^* =$

560   5. In this case, radial diffusion will become stronger only when a peak has started

561   forming due to chorus waves. However, in the simulation where State 2 is used, radial

562   diffusion will be strong from the beginning since significant peak in the PSD L^*-profile

563   exists initially.

564

5.3. Boundary condition

566   The outer boundary condition is an important parameter in the simulation. We chose to

567   use a characteristic energy of 2 keV for the plasma sheet which is the average value

568   measured at geosynchronous orbit [*Joseph Borovsky*, private communication 2007].

569   However, at geosynchronous altitude- near $L^* = 6.6$- it is also measured that this

570   temperature increases when magnetic activity increases, taking values of up to 5 keV

571   [*Joseph Borovsky*, private communication 2007].

572   In this Section we investigate the sensitivity of the simulation results to the boundary

573   condition. For this we consider two additional boundary conditions: one expressed by a

574   similar kappa distribution with characteristic energy of 5 keV (similar to the one used in

575 *Varotsou et al.*, [2005]) and one obtained empirically from CRRES measurements (used

576 in radial diffusion studies [*Shprits and Thorne, 2004; Shprits et al.*, 2005; *Shprits et al.,*

577 *2006b*]). The latter is defined by an exponential fit of the average flux measured by

578 CRRES at $L^* = 7$ and it is given by the expression

579

580 $$J = 8222.6 * 10^3 \exp\left(- E \middle/ 0.141\right) \qquad (4)$$

581

582 Where J is the differential flux (in $cm^{-2}sr^{-1}MeV^{-1}s^{-1}$) and E is the kinetic energy of the

583 particle (in MeV). Differential fluxes at $L^* = 7$ are converted into PSD and then PSD

584 values are relaxed adiabatically to $L^* = 8$ by assuming that the particle's magnetic

585 moment is conserved. This assumption is based on the fact that only radial diffusion

586 occurs in the $L^* = 7-8$ region in the Salammbô code.

587   Both conditions are assumed to be constant with time like the one that was used in

588 simulations presented before (kappa distribution with $E_0 = 2$ keV). By keeping the

589 boundary condition constant we are able to clearly identify the effect of chorus waves on

590 the electron dynamics. The effect of a time dependent boundary condition is currently

591 being studied and will be presented in a future paper (see Discussion section).

592   The spectra of the three source conditions at the outer boundary are shown in Figure 14.

593 If a higher characteristic energy kappa distribution is considered, PSD of higher energies

594 increases and thus the $\partial f/\partial E$ values become smaller. As a result, we expect energy

595 diffusion to be less important for this case. The second boundary condition from CRRES

596 defines lower PSD values at low energies ($E < 100$ keV) and higher PSD values for $E =$

597 100 keV – 1 MeV, compared to those defined by the kappa distribution with $E_0 = 2$ keV.

598   We must note here that we extrapolated the CRRES spectrum for $E < 153$ keV since the

599   MEA detector only measured fluxes for energies higher than 153 keV. This may not be

600   the most realistic approach but provides us with another test case to study the effect of the

601   boundary condition on the MeV electron dynamics. To avoid any confusion we will call

602   this condition the modified CRRES boundary condition.

603   We have performed the same dynamic simulation as described in Section 4.2 for both

604   new boundary conditions. Results are presented in Figures 15 (a), (b) and (c) for 2100

605   MeV/G equatorial electrons for all three boundaries at times *T1* and *T2* of the dynamic

606   test-case simulation. First thing we observe is that all boundary conditions produce a

607   local peak in the PSD L^*-profile at time *T2* at similar locations- near $L^* = 5$. The most

608   important difference can be noted for the case when the modified CRRES condition is

609   used. For this case, the increase of PSD is less important than in the other two cases, even

610   though a higher energy source is defined. This is due to the fact that the energy spectrum

611   defined by this condition determines lower and flatter phase space densities at energies

612   lower than 100 keV. As a result, the source is smaller and the energy diffusion due to

613   chorus wave interactions weaker.

614   However, a higher energy spectrum at the source does not affect the amount of

615   energization. Differences observed between Figure 15(a) and (b) at time *T2* are due to the

616   difference in the initial states at time *T1* (see section 5.2).

617

618   **6. Discussion**

619   The conclusions of our study are clearly shown and supported throughout this paper,

620   however, our simulations have important limitations. One of the first and most important

621   assumptions that we made was that chorus waves are confined near the equator. Adding

622   the effect of chorus waves at higher latitudes will affect the acceleration rate of electrons

623   but also their losses since losses are mostly determined by the value of $D\alpha\alpha$ near the edge

624   of the loss cone [*Shprits et al.,* 2006a]. Various observations have shown that chorus

625   waves are present at higher latitudes [*Tsurutani and Smith*, 1977; *Meredith et al.*, 2003b].

626   *Meredith et al*. [2003b] used CRRES data to show that dayside chorus waves are mostly

627   confined to higher latitudes ($\lambda > 15$ degrees) in contrast to night side chorus which are

628   mostly confined near the equator. When *Li et al.* [2007] introduced dayside high latitude

629   chorus (parallel propagating only), together with night side equatorial chorus, into their

630   2D simulations MeV losses at high latitudes became important, however the net result

631   was still electron acceleration.

632   Another limitation of our simulation is imposed by the fact that energy and pitch angle

633   diffusion coefficients due to chorus interactions are limited to a certain L^* space. Recent

634   observations have shown that chorus wave emissions can be detected at L^* shells up to

635     $L^* = 10$ [*Santolík et al.*, 2005], however in our simulations they are confined at $L^* < 6.5$.

636   This prevents us from estimating the relative power of chorus interactions and radial

637   diffusion outside $L^* = 6.2$, which is the last grid point inside $L^* = 6.5$ in Salammbô.

638   In addition, diffusion coefficients due to chorus interactions are defined for three Kp

639   categories: $Kp < 2$, $2 \leq Kp < 4$ and $Kp \geq 4$. The first two categories are small but the third

640   one is very broad (from 4 to 9) and it is the one that interests us the most. This broad

641   categorization is due to limited statistics for $Kp \geq 4$. However, radial diffusion

642   coefficients continuously increase with increasing geomagnetic activity. The Kp

643   categorization for the chorus wave effect makes it hard to directly compare with the

644   radial diffusion effect, especially if we want to simulate higher than $Kp = 4$ storms.

645   The precision of the Kp parameterization of wave intensity and f_{pe}/f_{ce} using the CRRES

646   data can also be questioned. In the first half of the mission, when the satellite was on the

647   dayside (at dawn), activity was weak, however, on the second half of the mission, when

648   the satellite was on the night side (at dusk), activity was high. For this second part, chorus

649   activity for low Kp values may be overestimated. In addition, as it can be seen in Figure 1

650   of *Meredith et al.* [2003b], there exists an important data gap above $L^* = 5$ near $MLT =$

651   10.

652   These limitations are also pointed out by *Maget et al.* [2007] when they run the

653   Salammbô 3D code using data assimilation techniques and found that when they included

654   chorus wave interactions in the scheme, fluxes were overestimated in the region inside L

655    $= 4$ as compared to the CRRES data.

656   More wave observations are needed for the better definition and understanding of the

657   region where chorus waves are interacting with electrons, their relation to magnetic

658   activity and their propagation characteristics. Many current observational studies focus

659   on the determination of the source and spatial distribution of chorus emissions using data

660   from POLAR [*Kristine Sigsbee*, private communication 2007], CLUSTER and DOUBLE

661   STAR [*Santolík et al.*, 2004, 2005]. More data will be available in the future with the

662   upcoming Radiation Belt Storm Probes mission.

663   We also think that the dependence of radial diffusion coefficients on energy and pitch

664   angle need to be further investigated. In the work presented here we chose to use the

665   diffusion coefficients estimated by *Brautigam and Albert* [2000] since these are the

666   values generally used by the radiation belt community. These coefficients depend on *L*-

667   shell and magnetic activity (*Kp* parameter). *Varotsou et al.* [2005] used radial diffusion

668   coefficients based on calculations by *Schulz* [1991] that are energy, pitch angle and L

669   dependent. A magnetic activity dependence was added based on a calculation using data

670   from the CRRES satellite. Magnetic radial diffusion coefficients by *Schulz* [1991]

671   become ~ 7 times weaker at α_{eq} = 20 degrees compared to their equatorial values. Thus,

672   results presented in this paper are similar to the ones presented by *Varotsou et al.* [2005]

673   for equatorial mirroring particles but different results are obtained for low α_{eq} values (not

674   shown in *Varotsou et al.* [2005]). In the case where coefficients by *Schulz* [1991] are

675   used, we don't observe the decrease at α_{eq} < 30 degrees, as seen in Figure 8, in Section

676   4.2.2. Recently, *Perry et al.* [2005] calculated radial diffusion coefficients by

677   incorporating spectral characteristics of Pc5 waves into 3D simulations using the guiding

678   center approximation. They found that when a data-based, frequency and *L*-dependent

679   model is used for the wave power, an important decrease in radial diffusion coefficients

680   occurs as the mirror latitude increases from 0 degrees (equator) to 20 degrees.

681   Finally, we must note the absence of the cross diffusion coefficient $D_{\alpha E}$ in equation (2).

682   The effect of this coefficient on the final result is still a subject of discussion. The high

683   values of the coefficient as calculated by the PADIE code [*Glauert and Horne*, 2005]-

684   sometimes even higher than the energy diffusion coefficient- suggest that its effect will

685   be important. A recent study by *Albert and Young* [2005] showed that when the cross

686   term is introduced in the diffusion equation results are qualitatively similar, but for small

687   α_{eq} energy diffusion is overestimated if the cross diffusion is neglected. The cross

688   diffusion term is not included in any current 3D radiation belt code.

689   Our current priority is to validate the new code by simulating a real storm. A more

690   realistic study of the radiation belt dynamics during geomagnetic storm conditions, where

691   the *Kp* and boundary variation are taken from real data, is currently being performed and

692   will be presented in a future paper.

693   Another important development of our code is the introduction of higher latitude day

694   side chorus. As discussed above, these waves are expected to introduce MeV electron

695   losses into the loss cone.

696   In addition, other wave types are currently being studied for introduction in the

697   Salammbô code. Recent studies have shown that enhanced EMIC waves in plasmaspheric

698   plumes formed during the storm's main phase (e.g., *Erlandson and Ukhorskiy*, 2001) can

699   cause strong MeV electron losses from pitch angle diffusion in the loss cone (*Thorne and*

700   *Kennel*, 1971; *Albert*, 2003; *Summers and Thorne*, 2003). Plasmaspheric hiss is currently

701   included in the code but it is independent of geomagnetic activity. Our current goal is to

702   introduce activity dependent hiss, since studies have shown that hiss is enhanced during

703   active conditions [*Meredith et al.,* 2004].

704   Finally, we want to underline the importance of comparing results obtained from

705   different codes. We hope that in the future we will be able to work with other teams in

706   comparing simulation results. However this has to be done with much caution since the

707   assumptions considered in each model are different.

708

709   **7. Conclusions**

710   We have run steady state and dynamic test-case simulations to study the effect of

711   electron-chorus resonant interactions on the radiation belt electron dynamics. We used

712 the Salammbô 3D physical model which includes radial diffusion and particle-wave

713 interactions inside and outside of the plasmasphere. Simulations were performed where

714 both electron-chorus interactions and radial diffusion were included in the code but we

715 also run simulations with only one of the two processes included. In that way we were

716 able to identify the role of each of these two key physical processes on the radiation belt

717 dynamics. The main results of our study are the following:

718   1. The introduction of chorus interactions in the Salammbô code leads to the local

719   acceleration of electrons to MeV energies.

720   2. Acceleration during dynamic test-case simulations of moderate activity conditions

721   ($Kp = 4$) is stronger at $L^* \sim 5$ and for equatorial pitch angles near 90 degrees.

722   3. The net effect of a geomagnetic storm- the peak value and location- is defined by

723   the relative power between chorus interactions and radial diffusion.

724   4. Simulation results are not sensitive to the high energy distribution of the source,

725   however they are sensitive to the low energy distribution ($E < 100$ keV).

726   Our results support the following scenario: during active geomagnetic periods low

727 energy electrons are transported inwards from an outer source location by enhanced

728 convection and radial diffusion, a fraction of them are energized locally to MeV energies

729 by chorus interactions. At the same time radial diffusion acts diffusing particles inwards

730 and outwards from the peak that tends to form in the PSD distribution.

33

731 **References**

732 Abel, B. and R. M. Thorne (1998a), Electron scattering loss in Earth's inner

733   magnetosphere 1. Dominant physical processes, *J. Geophys. Res., 103,* 2385.

734 Abel, B. and R. M. Thorne (1998b), Electron scattering loss in Earth's inner

735   magnetosphere 2. Sensitivity to model parameters, *J. Geophys. Res., 103,* 2397.

736 Albert, J. M., and S. L. Young (2005), Multidimensional quasi-linear diffusion of

737   radiation belt electrons, *Geophys. Res. Lett.*, *32*, L14110, doi:10.1029/2005GL023191.

738 Anderson, R. R., D. A. Gurnett, and D. L. Odem (1992), CRRES plasma wave

739   experiment, *J. Spacecr. Rockets*, *29*,(4), 570-573.

740 Beutier, T., and D. Boscher (1995), A three-dimensional analysis of the electron radiation

741   belt by the Salammbô code, *J. Geophys. Res., 100*, 14,853.

742 Beutier, T., D. Boscher, and Martin France (1995), SALAMMBO: A three-dimensional

743   simulation of the proton radiation belt, *J. Geophys. Res., 100*, 17,181.

744 Bourdarie, S., D. Boscher, T. Beutier, J.-A. Sauvaud, and M. Blanc (1996), Magnetic

745   storm modeling in the Earth's electron belt by the Salammbô code, *J. Geophys. Res.,*

746   *101*, 27,171-27,176.

747 Brautigam, D. H., and J. M. Albert (2000), Radial diffusion analysis of outer radiation

748   belt electrons during the October 9, 1990, magnetic storm, *J. Geophys. Res.*, *105*, 291.

749 Brizard, A. J., and Chan, A. A. (2001), Relativistic bounce-averaged quasi-linear

750   diffusion equation for low frequency electromagnetic fluctuations, *Phys. Of Plasmas*,

751   Vol. 8, 11, doi:10.1063/1.1408623.

752 Carpenter, D. L., and C. G. Park (1973), On what ionosphere workers should know about

753   the plasmapause-plasmasphere, *Rev. Geophys., 11*, 133.

754   Chen, Y., R. H. W. Friedel, and G. D. Reeves (2006), Phase space density distributions of

755   energetic electrons in the outer radiation belt during two Geospase Environment

756   Modeling Inner Magnetosphere/Storms selected storms, J. *Geophys. Res., 111*,

757   A11S04, doi:10.1029/2006JA011703.

758   Chen, Y., G. D. Reeves and R. H. W. Friedel (2007), The energization of relativistic

759   electrons in the outer Van Allen radiation belt, *Nature Physics*, doi:10.1038/nphys655.

760   Christon, S. P., D. G. Mitchell, D. J. Williams, L. A. Frank, C. Y. Huang, and T. E.

761   Eastman (1988), Energy spectra of plasma sheet ions and electrons from ~50eV/e to ~1

762   MeV during plasma temperature transitions, *J. Geophys. Res., 93*, 2562.

763   Christon, S. P., D. J. Williams, D. G. Mitchell, C. Y. Huang, and L. A. Frank (1991),

764   Spectral characteristics of plasma sheet ion and electron populations during disturbed

765   geomagnetic conditions, *J. Geophys. Res., 96*, 1.

766   Courant, R., K. Friedrichs, and H. Lewy (1967), On the Partial Difference Equations of

767   Mathematical Physics, *IBM J.* 11, 215-234.

768   Elkington, S. R., M. K. Hudson, and A. A. Chan (1999), Acceleration of relativistic

769   electrons vis drift-resonant interaction with toroidal-mode Pc-5 ULF oscillations,

770   *Geophys. Res. Lett., 26*, 3273-3276.

771   Fälthammar, C.G. (1965), Effects of time-dependent electric fields on geomagnetically

772   trapped radiation, *J. Geophys. Res., 70*, 2503.

773   Fälthammar, C.G. (1966), On the transport of trapped particles in the outer

774   magnetosphere, *J. Geophys. Res., 71*, 1487.

775   Fox, N. J., B. H. Mauk, and J. B. Blake (2006), Role of non-adiabatic processes in the

776   creation of the outer radiation belts, *Geophys. Res. Lett., 33*, L18108, doi:10.1029/2006GL026598.

777   doi:10.1029/2006GL026598.

778   Friedel, R. H., G. D. Reeves, and T. Obara (2002), Relativistic electron dynamics in the

779   inner magnetosphere- A review, *J. Atmos. Sol. Terr. Phys.*, *64*, 265.

780   Glauert, S. A. and R. B. Horne (2005), Calculation of pitch angle and energy diffusion

781   coefficients with the PADIE code, *J. Geophys. Res., 110*, doi:10.1029/2004JA010851.

782   Green, J. C., and M. G. Kivelson (2004), Relativistic electrons in the outer radiation belt:

783   Differentiating between acceleration mechanisms, *J. Geophys. Res., 109*, A03213,

784   doi:10.1029/2003JA010153.

785   Hedin, A. E. (1979), Tables of thermospheric temperature, density and composition

786   derived from satellite and ground based measurements, *Rep. N79-18515, vol.1-3*,

787   NASA Goddard Space Flight Center, Greenbelt, Md.

788   Holzworth, R. H., and F. S. Mozer (1979), Direct evaluation of the radial diffusion

789   coefficient near L = 6 due to electric field fluctuations, *J. Geophys. Res.*, *84*, 2559.

790   Horne, R. B. (2002), The contribution of wave particle interactions to electron loss and

791   acceleration in the Earth's radiation belts during geomagnetic storms, in *USRI Review*

792   *of Radio Science 1999-2002*, edited by W. R. Stone, pp. 801-828, chap. 33, John Wiley,

793   Hoboken, N. J.

794   Horne, R. B., and R. M. Thorne (1998), Potential waves for relativistic electron scattering

795   and stochastic acceleration during magnetic storms, *Geophys. Res. Lett.*, *25,* 3011.

796 Horne, R. B., S. A. Glauert, and R. M. Thorne (2003a), Resonant diffusion of radiation

797   belt electrons by whistler-mode chorus, *Geophys. Res. Lett., 30*, 1493,

798   doi:10.1029/2003GL016963.

799 Horne, R. B., N. P. Meredith, R. M. Thorne, D. Heynderickx, R. H. A. Iles, and R. R.

800   Anderson (2003b), Evolution of energetic electron pitch angle distributions during

801   storm time electron acceleration to megaelectronvolt energies, *J. Geophys. Res., 108*,

802   1016, doi:10.1029/2001JA009165.

803 Horne, R. B., R. M. Thorne, Y. Y. Shprits, N. P. Meredith, S. A. Glauert, A. J. Smith, S.

804   G. Kanekal, D. N. Baker, M. J. Engebretson, J. L. Posch, M. Spasojevic, U. S. Inan, J.

805   S. Pickett, and P. M. E. Decreau (2005), Wave acceleration of electrons in the Van

806   Allen radiation belts, *Nature*, Vol 437, doi:10.1038/nature03939.

807 Jordanova, V. K., L. M. Kistler, J. U. Kozyra, G. V. Kazanov, and A. F. Nagy (1996),

808   Collisional losses of ring current ions, *J. Geophys. Res.*, *101*, 111.

809 Jordanova, V. K., A. Boonsiriseth, R. M. Thorne, and Y. Dotan (2003), Ring current

810   asymmetry from global simulations using a high-resolution electric field model, *J.*

811   *Geophys. Res.*, *108*(A12), 1443, doi:10.1029/2003JA009993.

812 Jordanova, V. K., and Y. S. Miyoshi (2005), Relativistic model of ring current and

813   radiation belt ions and electrons: Initial results, *Geophys. Res. Lett.*, *32*, L14104,

814   doi:10.1029/2005GL023020.

815 Iles, R. H. A., N. P. Meredith, A. N. Fazakerley, and R. B. Horne (2006), Phase space

816   density analysis of the outer radiation belt energetic electron dynamics, *J. Geophys.*

817   *Res.*, *111*, A03204, doi:10.1029/2005JA011206.

818 Kennel, C. F. (1969), Consequences of a magnetospheric plasma, *Rev. Geophys., 7*, 379.

819   Kennel, C. F., and F. Engelmann (1966), Velocity space diffusion from weak plasma

820   turbulence in a magnetic field, *Phys. Fluids, 9*, 2377.

821   Lanzerotti,L. J., and C. G. Morgan (1973), ULF geomagnetic power near L = 4-2:

822   Temporal variation of the radial diffusion coefficient for relativistic electrons, *J.*

823   *Geophys. Res.*, *78*,4600.

824   Lanzerotti, L. J., C. G. MacLennan, and M. Schulz (1970), Radial diffusion of outer-zone

825   electrons: An empirical approach to third-invariant violation, *J. Geophys. Res.*, *75*,

826   5351.

827   Li, X. (2004), Variations of 0.7-6.0 MeV electrons at geosynchronous orbit as a function

828   of solar wind, *Sp. Weather*, Vol. 2, No. 3, S0300610.1029/2003SW000017.

829   Li, W., Y. Y. Shprits, and R. M. Thorne (2007), Dynamic evolution of energetic outer

830   zone electrons due to wave-particle interactions during storms, *J. Geophys. Res.*,

831   accepted.

832   Lyons, L. R. (1974), General relations for resonant particle diffusion in pitch angle and

833   energy, *J. Plasma Phys., 12*, 45-49.

834   Maget, V., S. Bourdarie, D. Boscher, and R. H. W. Friedel (2007), Data assimilation of

835   LANL satellite data into the Salammbô electron code over a complete solar cycle by

836   direst insertion, *Sp. Weather*, 2007SW000322.

837   McIlwain, C.E. (1961), Coordinates for mapping the distribution of magnetically trapped

838   particles, *J. Geophys. Res., 66*, 3681-3691.

839   Meredith, N. P., R. B. Horne, and R. R. Anderson (2001), Substorm dependence of

840   chorus amplitudes: Implications for the acceleration of electrons tp relativistic energies,

841   *J. Geophys. Res.*, *106*, 13,165.

842   Meredith, N. P., R. B. Horne, R. H. A. Iles, R. M. Thorne, D. Heyndrickx, and R. R.

843   Anderson (2002a), Outer zone relativistic electron acceleration associated with

844   substorm-enhanced whistler-mode chorus, *J. Geophys. Res., 107*, 1144.

845   Meredith, N. P., R. B. Horne, D. Summers, R. M. Thorne, R. H. A. Iles, D. Heynderickx,

846   and R. R. Anderson (2002b), Evidence for acceleration of outer zone electrons to

847   relativistic energies by whistler mode chorus, *Ann. Geophys., 20*, 967.

848   Meredith, N. P., M. Cain, R. B. Horne, R. M. Thorne, D. Summers, and R. R. Anderson

849   (2003a), Evidence for chorus-driven electron acceleration to relativistic energies from a

850   survey of geomagnetically-disturbed periods, *J. Geophys. Res., 108*(A6), 1248,

851   doi:10.1029/2002JA009764.

852   Meredith, N. P., R. B. Horne, R. M. Thorne, and R. R. Anderson (2003b), Favored

853   regions for chorus-driven electron acceleration to relativistic energies in the Earth's

854   outer radiation belt, *Geophys. Res. Lett., 30*, 1871, doi:10.1029/2003GL017698.

855   Meredith, N. P., R. B. Horne, R. M. Thorne, D. Summers, and R. R. Anderson (2004),

856   Substorm dependence of plasmaspheric hiss, *J. Geophys. Res., 109,* A06209,

857   doi:10.1029/2004JA010387.

858   Miyoshi, Y., A. Morioka, T. Obara, H. Misawa, T. Nagai, and Y. Kasahara (2003),

859   Rebuilding process of the outer radiation belt during the 3 November 1993 magnetic

860   storm: NOAA and Exos-D observations, *J.Geophys. Res., 108*(A1), 1004,

861   doi:10.1029/2001JA007542.

862   Miyoshi, Y. S., V. K. Jordanova, A. Morioka, M. F. Thomsen, G. D. Reeves, D. S.

863   Evans, and J. C. Green (2006), Observations and modeling of energetic electron

864   dynamics during the October 2001 storm, *J. Geophys. Res.*, *111*, A11S02,

865   doi:10.1029/2005JA011351.

866   Obara, T., T. Nagatsuma, M. Den, Y. Miyoshi, and A. Morioka (2000), Main-phase

867   creation of 'seed' electrons in the outer radiation belt, *Earth Planets Space, 52*, 41-47.

868   O'Brien, T. P., R. L. McPherron, D. Sornette, G. D. Reeves, R. H. Friedel, and H. J.

869   Singer (2001), Which magnetic storms produce relativistic electrons at geosynchronous

870   orbit?, *J. Geophys. Res.*, *106*(8), 15,533, doi:10.1029/2001JA000052.

871   Perry, K. L., M. K. Hudson, and S. R. Elkington (2005), Incorporating spectral

872   characteristics of Pc5 waves into three-dimensional radiation belt modeling and the

873   diffusion of relativistic electrons, *J. Geophys. Res.*, *110*, A03215.

874   Reeves, G. D., D. N. Baker, R. D. Belian, J. B. Blake, T. E. Cayton, J. F. Fennell, R. H.

875   W. Friedel, M. M. Meier, R. S. Selesnick and H. E. Spence (1998), The global response

876   of relativistic radiation belt electrons to the January 1997 magnetic cloud, *Geophys.*

877   *Res. Lett., 25*(17), 3265.

878   Reeves, G. D., K. L. McAdams, R. H. Friedel, and T. P. O'Brien (2003), Acceleration

879   and loss of relativistic electrons during geomagnetic storms, *Geophys. Res. Lett.*,

880   *30*(10), 1529, doi:10.1029/2002GL016513.

881   Roederer, J. G., Dynamics of Geomagnetically Trapped Radiation, Springer-Verlag, New

882   York, 1970.

883   Santolík, O., D. A. Gurnett, and J. S. Pickett (2004), Multipoint investigation of the

884   source region of storm-time chorus, *Ann. Geophys.*, 22, 2555-2563.

885   Santolík, O., E. Macúšová, K. H. Yearby, N. Cornilleau-Wenhrlin, and H. StC. K.

886   Alleyne (2005), Radial variation of whistler-mode chorus: first results from the

887   STAFF/DWP instrument on board the Double Star TC-1 spacecraft, *Ann. Geophys.*, 23,

888   2937-2942.

889   Schulz, M. (1991), The magnetosphere, geomagnetically trapped radiation, in

890   *Geomagnetism*, vol. 4, edited by J. A. Jacobs, pp. 202-256, Elsevier, New York.

891   Schulz, M., and L. Lanzerotti (1974), Particle Diffusion in the Radiation Belts, Springer,

892   New York.

893   Shprits, Y. Y., and R. M. Thorne (2004), Time dependent radial diffusion modeling of

894   relativistic electrons with realistic loss rates, *Geophys. Res. Lett., 31*, L08805,

895   doi:10.1029/2004GL019591.

896   Shprits Y. Y., and R. M. Thorne (2006a), Controlling effect of the pitch angle scattering

897   rates near the edge of the loss cone on the electron lifetime, *J. Geophys. Res.*, *111*,

898   A12206, doi:10.1029/2006JA011758.

899   Shprits Y. Y., R. M. Thorne, R. Friedel, G. D. Reeves, J. Fennell, D. N. Baker, S. G.

900   Kanekal (2006b), Outward radial diffusion driven by losses at the magnetopause, *J.

901   Geophys. Res.*, *111*, A11214, doi:10.1029/2006JA011657.

902   Shprits Y. Y., R. M. Thorne, R. B. Horne, S. A. Glauert, M Cartwright, C. T. Russel, D.

903   N. Baker, S. G. Kanekal (2006c), Acceleration mechanism responsible for the

904   formation of the new radiation belt during the 2003 Halloween solar storm, *Geophys.

905   Res. Lett*., *33*, L05104, doi:10.1029/2005GL024256.

906   Shprits, Y. Y., R. M. Thorne, G. D. Reeves, and R. H. Friedel (2005), Radial diffusion

907   modeling with empirical lifetimes: comparison with CRRES observations, *Ann.

908   Geophys.*, 23, 1467-1471.

909   Summers, D., R. M. Thorne, and F. Xiao (1998), Relativistic theory of wave-particle

910   resonant diffusion with application to electron acceleration in the magnetosphere, *J.*

911   *Geophys. Res., 103*, 20,487.

912   Thorne, R. M., E. J. Smith, K. J. Fiske, and S. R. Church (1974), Intensity variation of

913   ELF hiss and chorus during isolated substorms, *Geophys. Res. Lett., 1*, 193-196.

914   Tsurutani, B. T. and E. J. Smith (1977), Two types of magnetospheric chorus and their

915   substorm dependencies, *J. Geophys. Res.*, *82*, 5112.

916   Vacaresse, A, D. Boscher, S. Bourdarie, M. Blanc, and J.-A. Sauvaud (1999), Modeling

917   the high-energy proton belt, *J. Geophys. Res., 104*, 28,601.

918   Van Allen, J.A., G.H. Ludwig, E.C. Ray, and C.E. McIlwain (1958), Observations of

919   high intensity radiations by satellites 1958 alpha and gamma, *Jet. Propul.*, *28*, 588.

920   Varotsou, A., D. Boscher, S. Bourdarie, R. B. Horne, S. A. Glauert, and N. P. Meredith

921   (2005), Simulation of the outer radiation belt electrons near geosynchronous orbit

922   including both radial diffusion and resonant interaction with Whistler-mode chorus

923   waves, *Geophys. Res. Lett., 32*, L19106, doi:10.1029/2005GL023282.

924 **Figure captions**

925 **Figure 1.** Energy and pitch angle diffusion coefficients due to chorus interactions, as a

926 function of energy and equatorial pitch angle for three Kp categories at $L* = 4.8$.

927 **Figure 2.** Steady state phase space density calculation (in $MeV^{-3}s^{-3}$) for 2100 MeV/G

928 equatorial particles and $Kp = 1.3$, for two simulations: (a) including chorus wave

929 interactions and (b) including only radial diffusion.

930 **Figure 3.** Steady state phase space density (in $MeV^{-3}s^{-3}$) as a function of equatorial pitch

931 angle for 1.7 MeV electrons at $L* = 5.2$ and for $Kp = 1.3$, for two simulations: (a)

932 including chorus wave interactions (red line) and (b) including only radial diffusion (blue

933 line).

934 **Figure 4.** Energy and pitch angle diffusion coefficients (in s^{-1}) as a function of equatorial

935 pitch angle, for $L* = 5.2$, $E = 1.7$ MeV and $Kp = 1.3$.

936 **Figure 5.** Steady state phase space density (in $MeV^{-3}s^{-3}$) as a function of energy for

937 equatorial particles at $L* = 5.2$ and for $Kp = 1.3$, for two simulations: including chorus

938 wave interactions (red line) and including only radial diffusion (blue line).

939 **Figure 6.** Kp profile for the dynamic test-case simulation.

940 **Figure 7.** Phase space densities (in $MeV^{-3}s^{-3}$) for 2100 MeV/G equatorial electrons as a

941 function of $L*$ from the three simulations at time $T2$: including only chorus wave

942 interactions (orange line), including only radial diffusion (blue line) and including both

943 processes (red line), starting from the same initial state (black line). Dashed lines show

944 the position of the plasmapause for $Kp = 1.3$ and $Kp = 4$.

945 **Figure 8.** Phase space densities (in $MeV^{-3}s^{-3}$) for 1.7 MeV electrons at $L* = 5.2$ as a

946 function of equatorial pitch angle from the three simulations at time $T2$.

947   **Figure 9.** 2D plots of phase space densities at $L^* = 5.2$ as a function of energy (shown

948   from 0.5 to 5 MeV on a log scale) and equatorial pitch angle at a) time T1 and b) time

949   T2.

950   **Figure 10.** Diffusion coefficients as a function of energy for $Kp = 4$ and $L^* = 5.2$: (a)

951   pitch angle diffusion coefficients at $\alpha_{eq} = 85$ degrees (solid line) and 30 degrees (dash dot

952   line) and (b) energy diffusion coefficients at $\alpha_{eq} = 90$ degrees (solid line) and 30 degrees

953   (dash dot line).

954   **Figure 11.** Omnidirectional equatorial flux variation during the test-case simulation for

955   1.6 MeV electrons. The plasmapause position is marked with a green line.

956   **Figure 12.** Phase space densities (in $MeV^{-3}s^{-3}$) for 2100 MeV/G equatorial particles as a

957   function of L^* for (a) the three steady state simulations and (b) at time $T2$ for the three

958   dynamic simulations starting from the same initial state at $T1$ (black line).

959   **Figure 13.** Phase space densities (in $MeV^{-3}s^{-3}$) for 2100 MeV/G equatorial particles as a

960   function of L^* at times $T1$ and $T2$ from two dynamic simulations: one starting from State

961   1 and one starting from State 2.

962   **Figure 14.** Spectrum of the three distributions used as a source at the outer boundary (L^*

963   = 8): the kappa distribution with $E_0 = 2$ keV (red line), the kappa distribution with $E_0 = 5$

964   keV (blue line) and the modified CRRES distribution (black line).

965   **Figure 15.** Phase space densities (in $MeV^{-3}s^{-3}$) for 2100 MeV/G equatorial particles as a

966   function of L^* at times $T1$ and $T2$ using the three boundary conditions: (a) a kappa

967   distribution with $E_0 = 2$ keV, (b) the kappa distribution with $E_0 = 5$ keV and (c) the

968   modified CRRES distribution.

969 **Table1. Diffusive processes in Salammbô**

Physical Process (1)	Effect (2)	Coefficients (3)	Calculation (4)	Parameters (5)
Field fluctuations	Radial Diffusion	$D_{LL}^{(m)}$	*Brautigam and Albert* (2000)	*Brautigam and Albert* (2000)
Particle-wave interactions *inside* plasmasphere	Pitch angle diffusion	D_{yy}	*Abel and Thorne* (1998a)	Described in: *Abel and Thorne* (1998b)
Coulomb collisions with high atmosphere	Pitch angle diffusion	D_{yy}	*Schulz and Lanzerotti (1974)*	Atmospheric densities from MSIS 86 model[a] [*Hedin*, 1979]
Particle-wave interactions *outside* plasmasphere	Energy diffusion and pitch angle diffusion	D_{EE}, D_{yy}	PADIE code: *Glauert and Horne* (2005)	CRRES data: Glauert and Horne (2005) and Meredith et al. (2003b)

970 [a] Plus a hydrostatic model above 800 km for each species

971

972 **Table 1.** Physical processes included in Salammbô, their effect on radiation belt

973 electrons, the coefficients that express their effect in the diffusion equation and the

974 references for the calculation and the parameters used to estimate the coefficients.

975 **Table 2. Chorus wave characteristics**

Parameter	Assumed distribution	Characteristic values
Wave power	Gaussian distribution	Peak: $0.35f_{ce}$ Bandwidth: $0.15fce$ Lower cut-off: $0.125fce$ Upper cut-off: $0.575fce$
Wave normal angle	Gaussian distribution $X = \tan(\psi)$	Peak: $X_m = 0$ Angular spread: $X_w = \tan(30^0)$ $X_{min} = 0$ $X_{max} = 1$

976

977 **Table 2.** The wave characteristics used for the calculation of the pitch angle and energy

978 diffusion coefficients due to chorus wave interactions.

979 **Table 3. Diffusive processes outside the plasmapause**

Diffusive process	Coefficients	Domain of application
Radial Diffusion	$D_{LL} = 10^{(0.506Kp-9.325)} L^{10}$	applied everywhere in our simulation domain
Pitch-angle and energy diffusion due to chorus waves	PADIE coefficient matrix for $D_{\alpha\alpha}$ and D_{EE} for 3 Kp categories	Plasmapause $< L \leq 6.5$ 10 keV $\leq E \leq$ 3MeV all α_{eq} values

980

981 **Table 3.** The two diffusive physical processes included in Salammbô outside the

982 plasmapause, their expressions and the simulation domain of application.
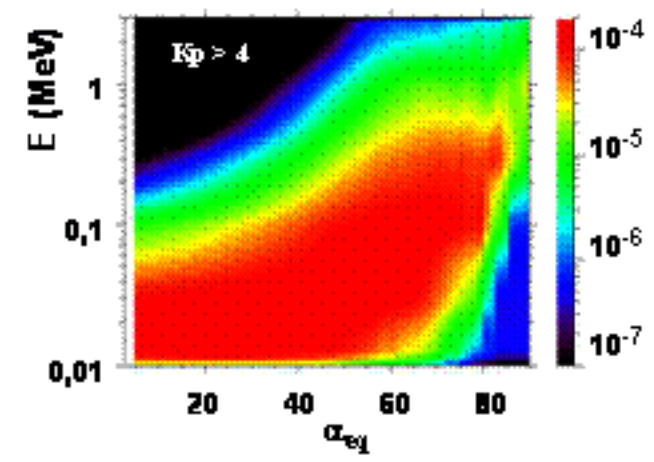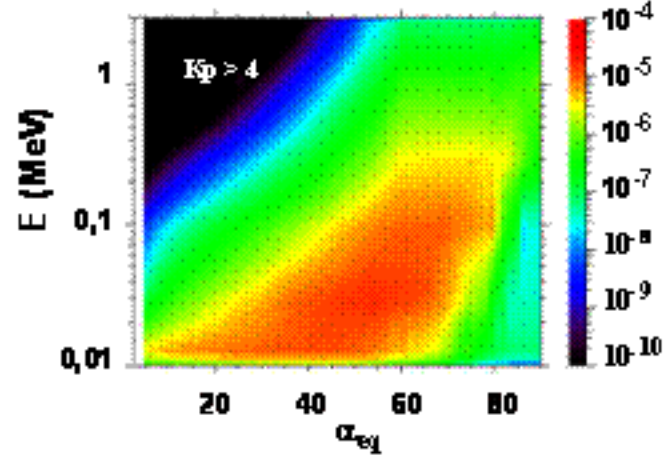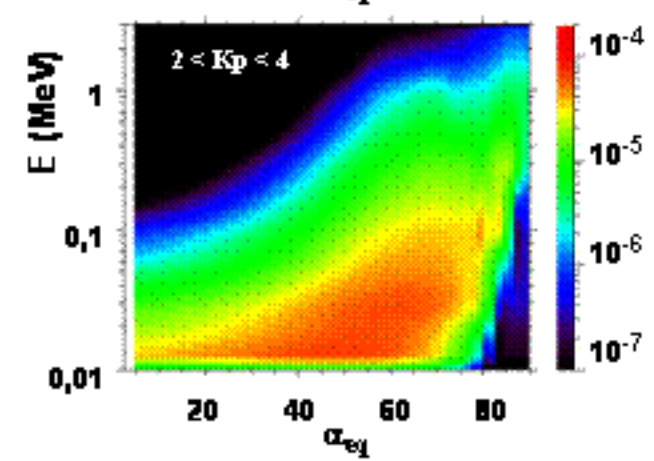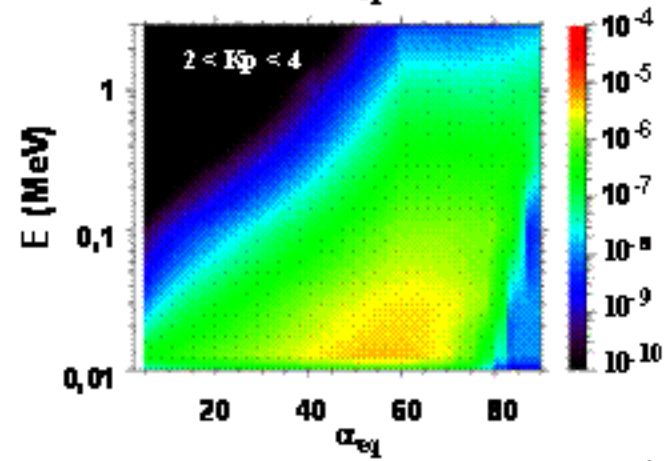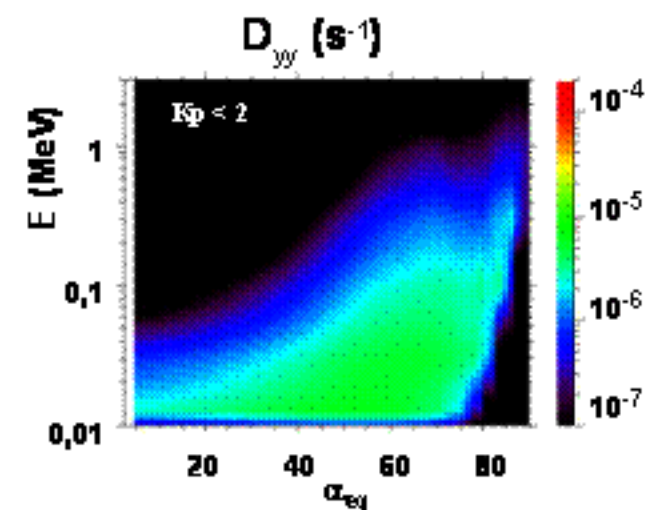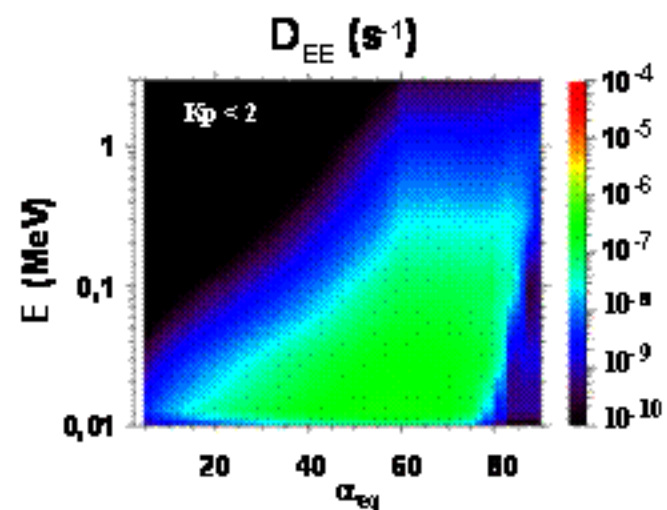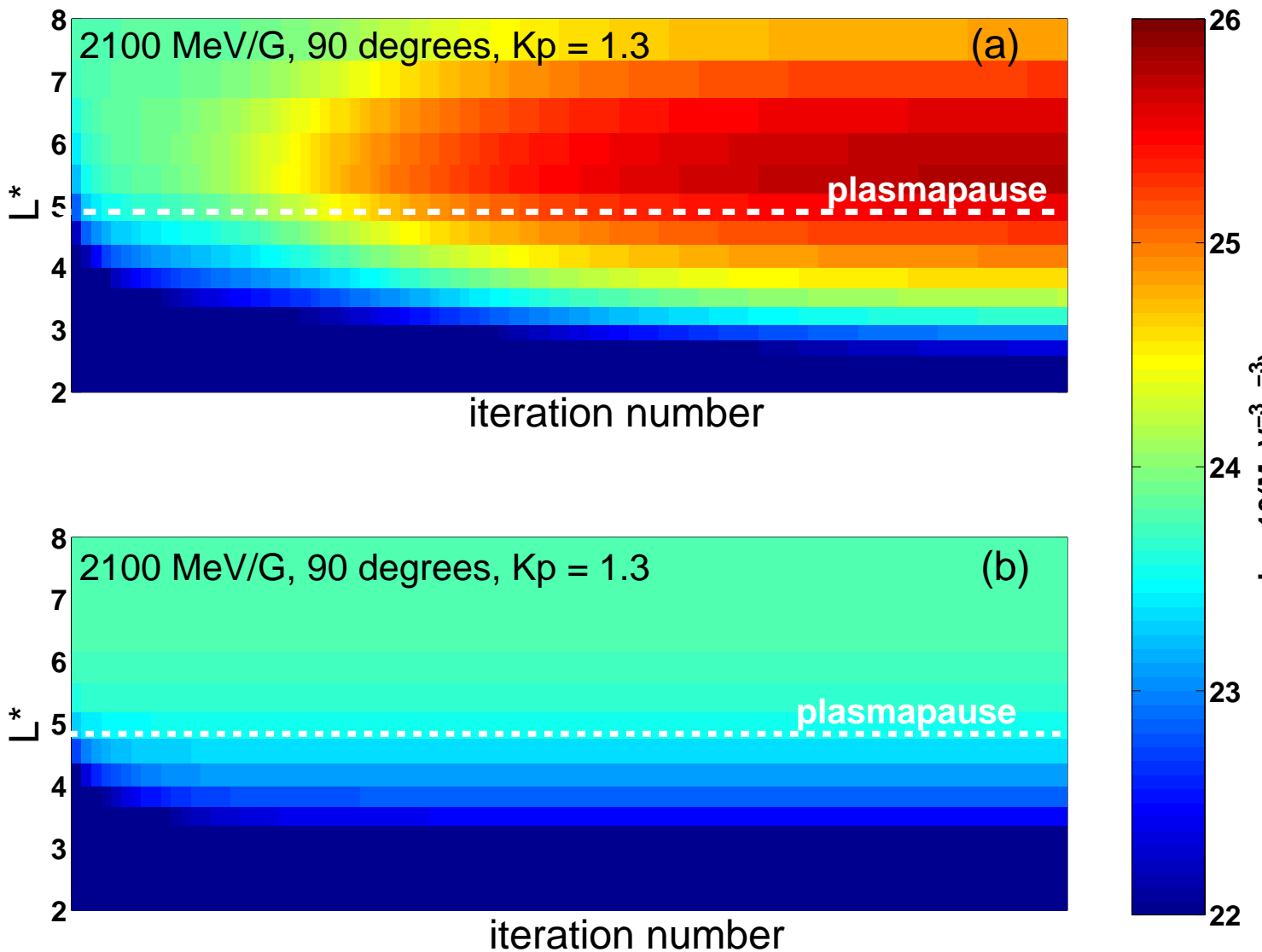
D_{EE} (s^{-1})

$D_{\gamma\gamma}$ (s^{-1})

Figure 2. Steady state phase space density calculation (in MeV−3 s−3) for 2100 MeV/G equatorial particles and Kp = 1.3, for two simulations: (a) including chorus wave interactions and (b) including only radial diffusion.
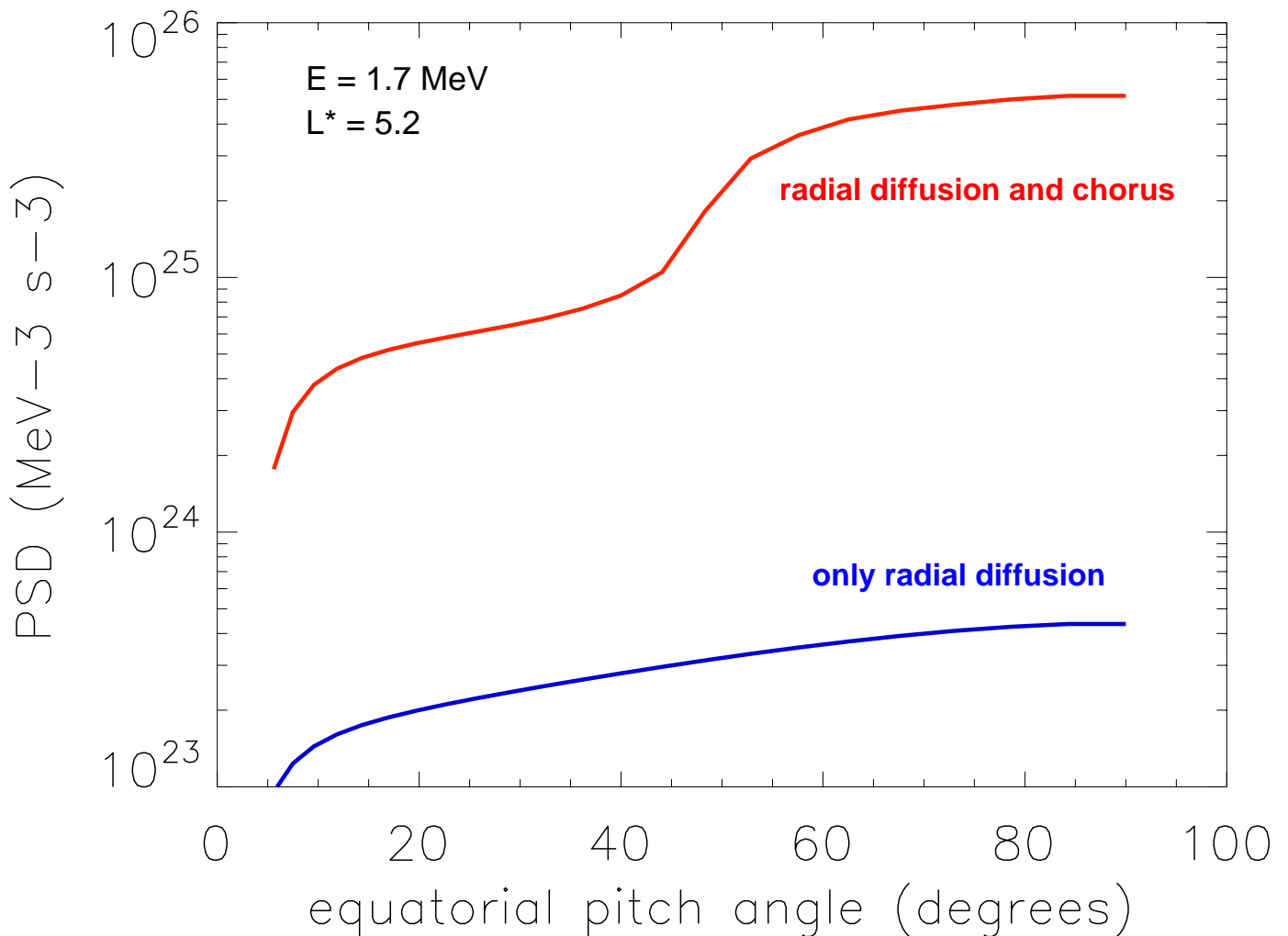
Figure 3. Steady state phase space density as a function of equatoral pitch angle for 1.7 MeV electrons at L* = 5.2 and for Kp = 1.3, for two simulations: (a) including chorus wave interactions (red line) and (b) including only radial diffusion (blue line).
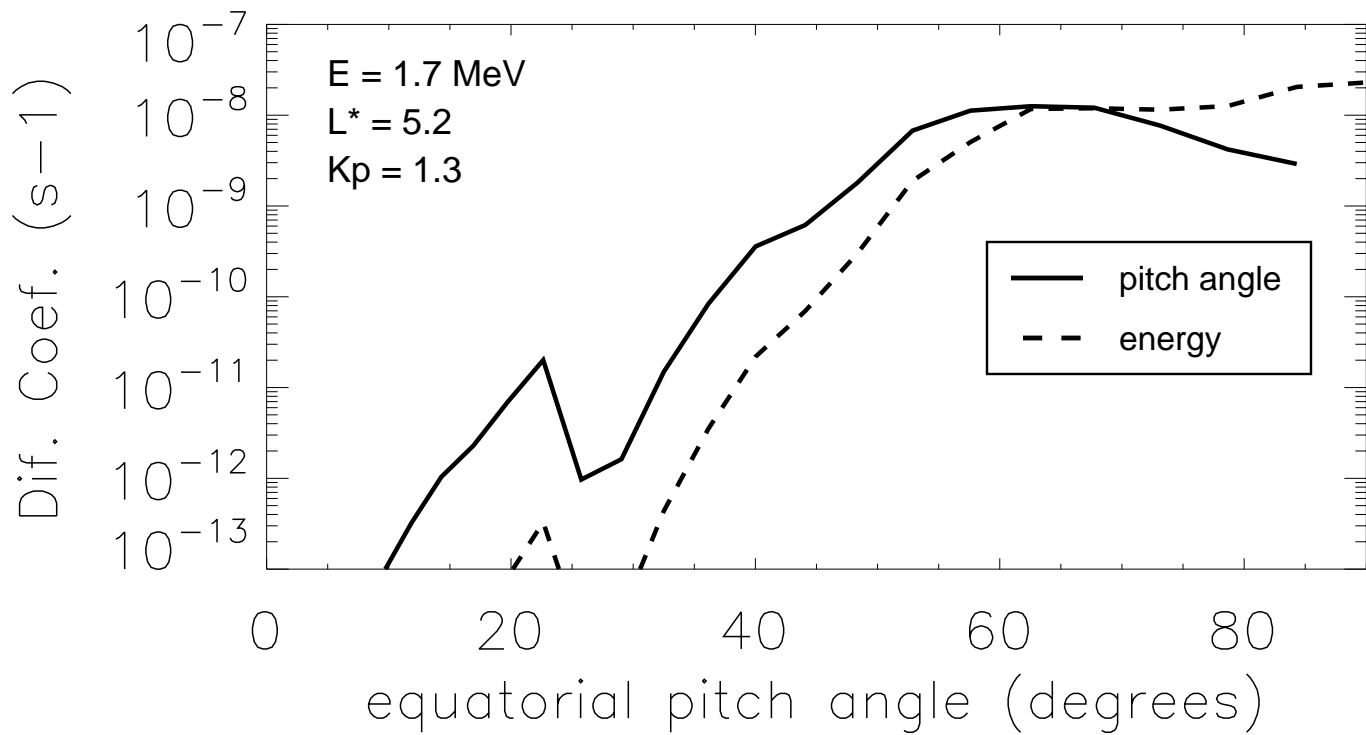
Figure 4. Energy and pitch angle diffusion coefficients (in s−1) as a function of equatorial pitch angle, for L* = 5.2, E = 1.7 MeV and Kp = 1.3.
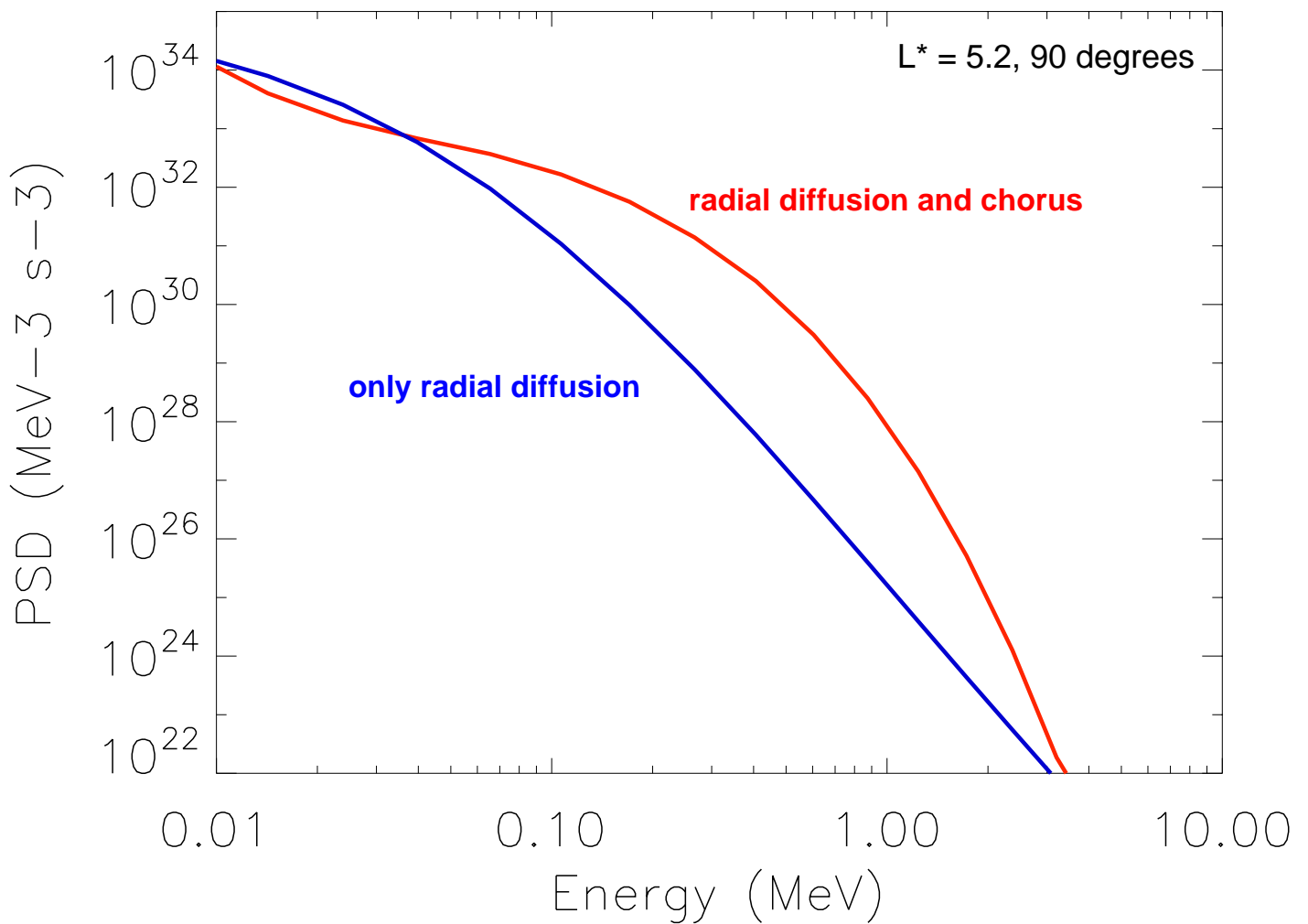
Figure 5. Steady state phase space density (in MeV−3 s−3) as a function of energy for equatorial particles at L* = 5.2 and for Kp = 1.3, for two simulations: including chorus wave interactions (red line) and including only radial diffusion (blue line).
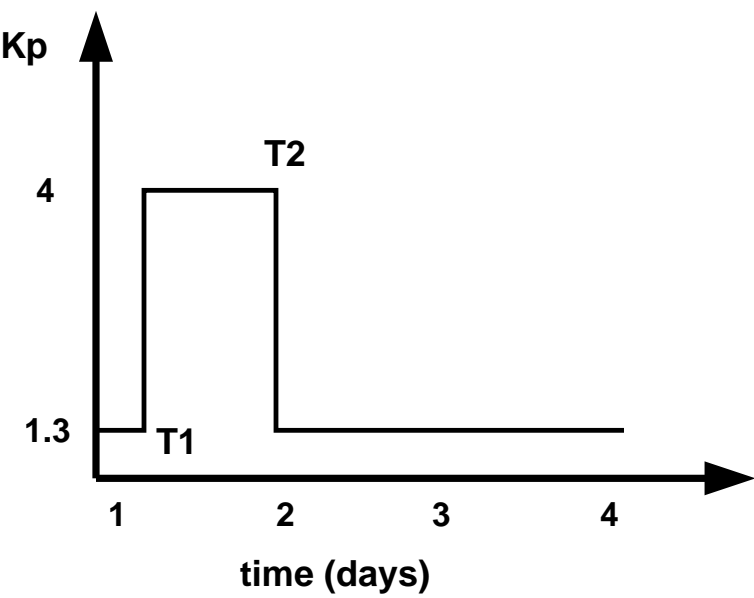
Figure 6. Kp profile for the dynamic test case simulation.
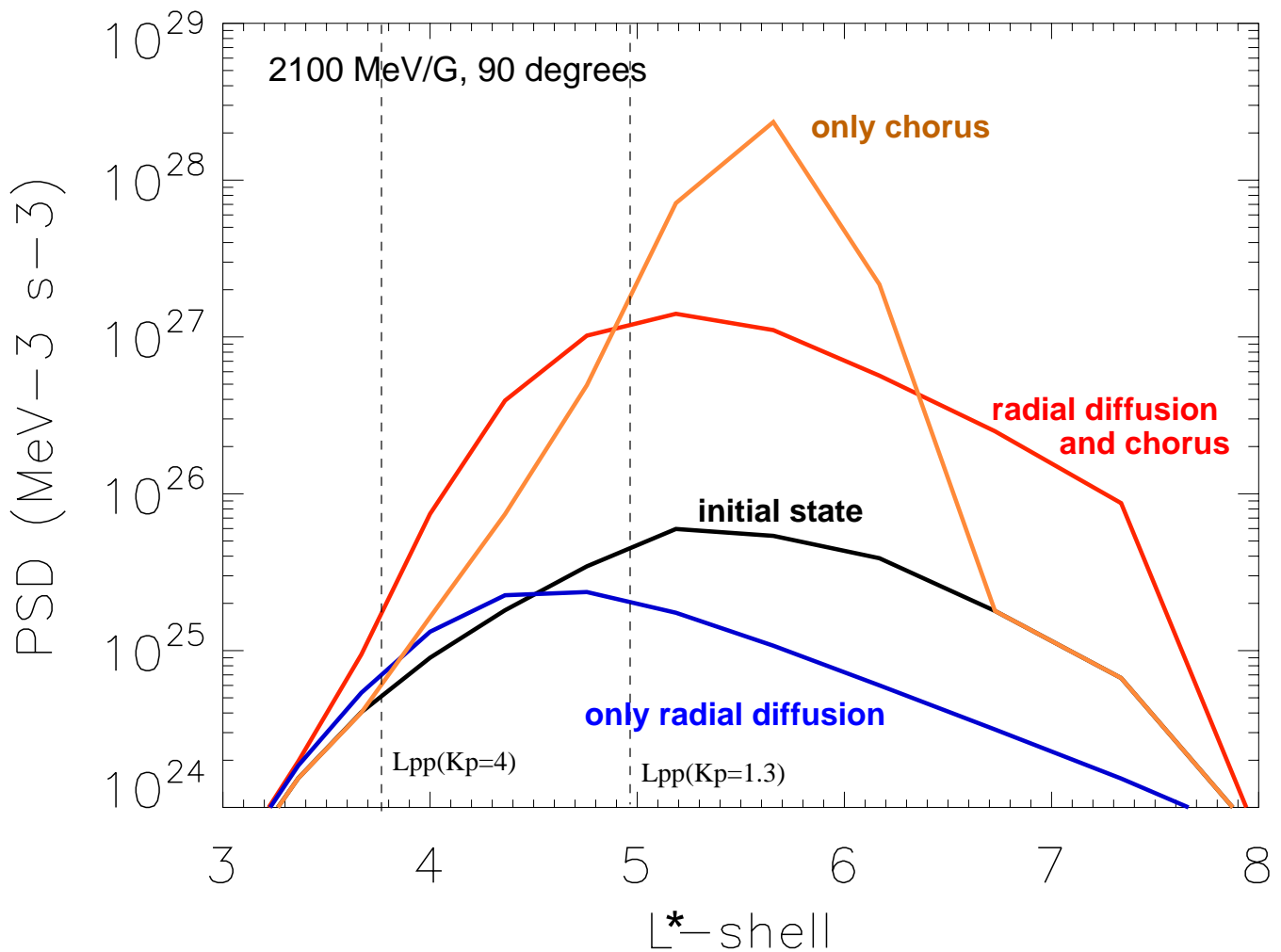
Figure 7. Phase Space densities (in MeV−3 s−3) for 2100 MeV/G equatorial particles as a function of L* from the three simulations at time T2: including only chorus wave interactions (orange line), including only radial diffusion (blue line) and including both processes (red line), starting from the same initial state (black line. Dashed lines show the position of the plasmapause for Kp = 1.3 and Kp = 4.
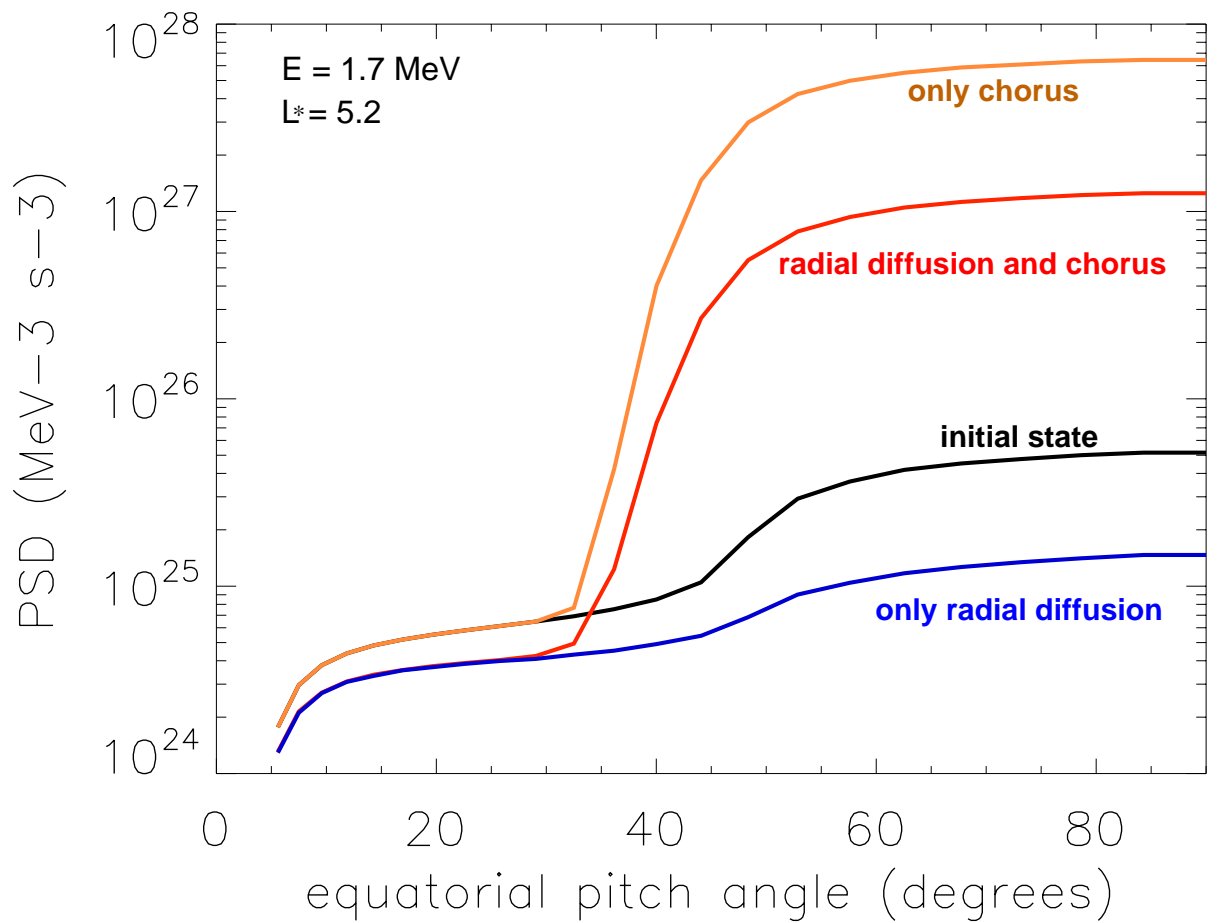
Figure 8. Phase space densities for 1.7 MeV electrons at L* = 5.2 as a function of equatorial pitch angle from the three simulations at time T2: including only chorus wave interactions (orange line), including only radial diffusion (blue line) and including both processes (red line),starting from the same initial state (black line).
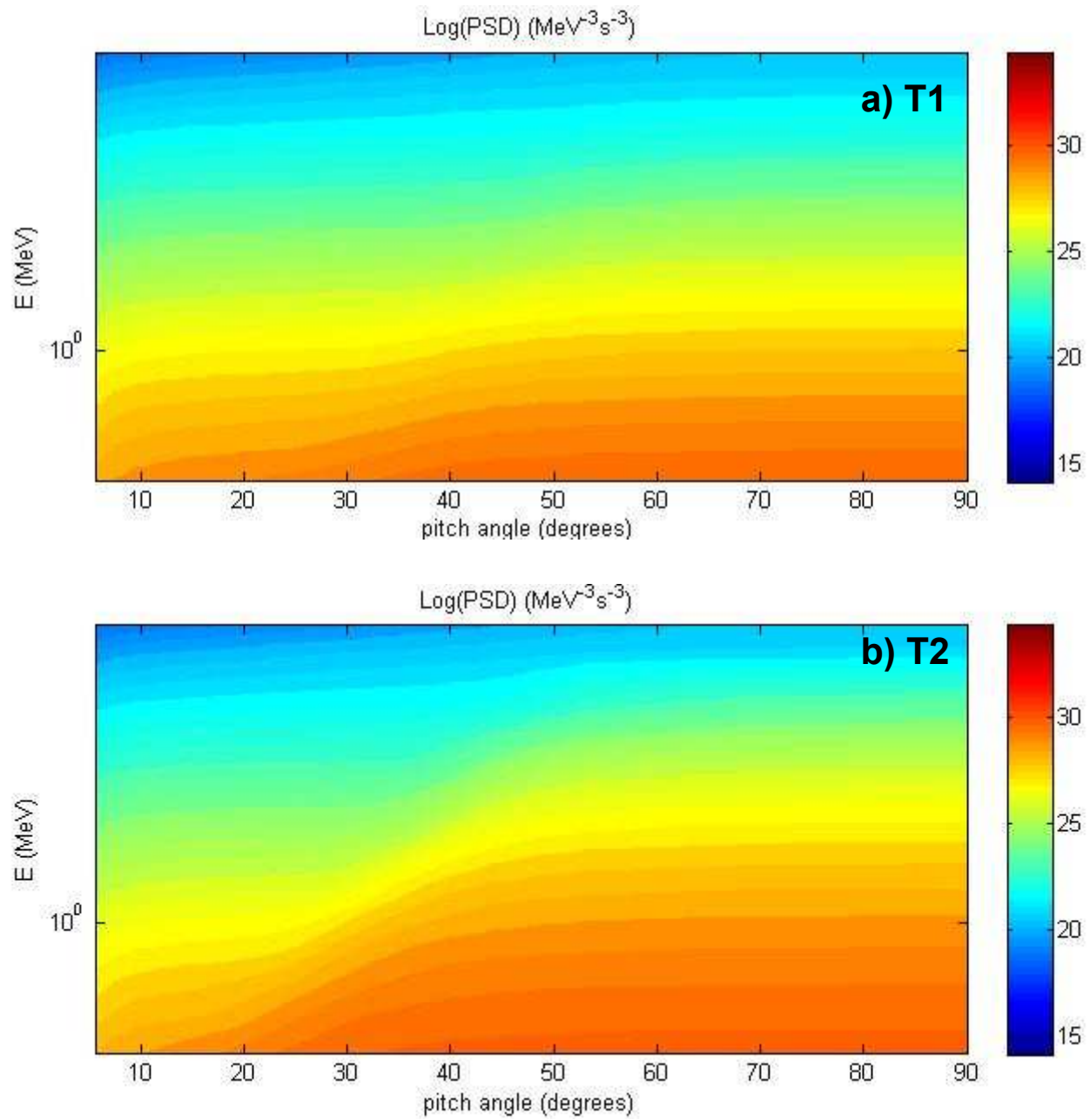
Figure 9. 2D plots of phase space densities at $L^* = 5.2$ as a function of energy (shown from 0.5 to 5 MeV on a log scale) and equatorial pitch angle at a) time T1 and b) time T2.
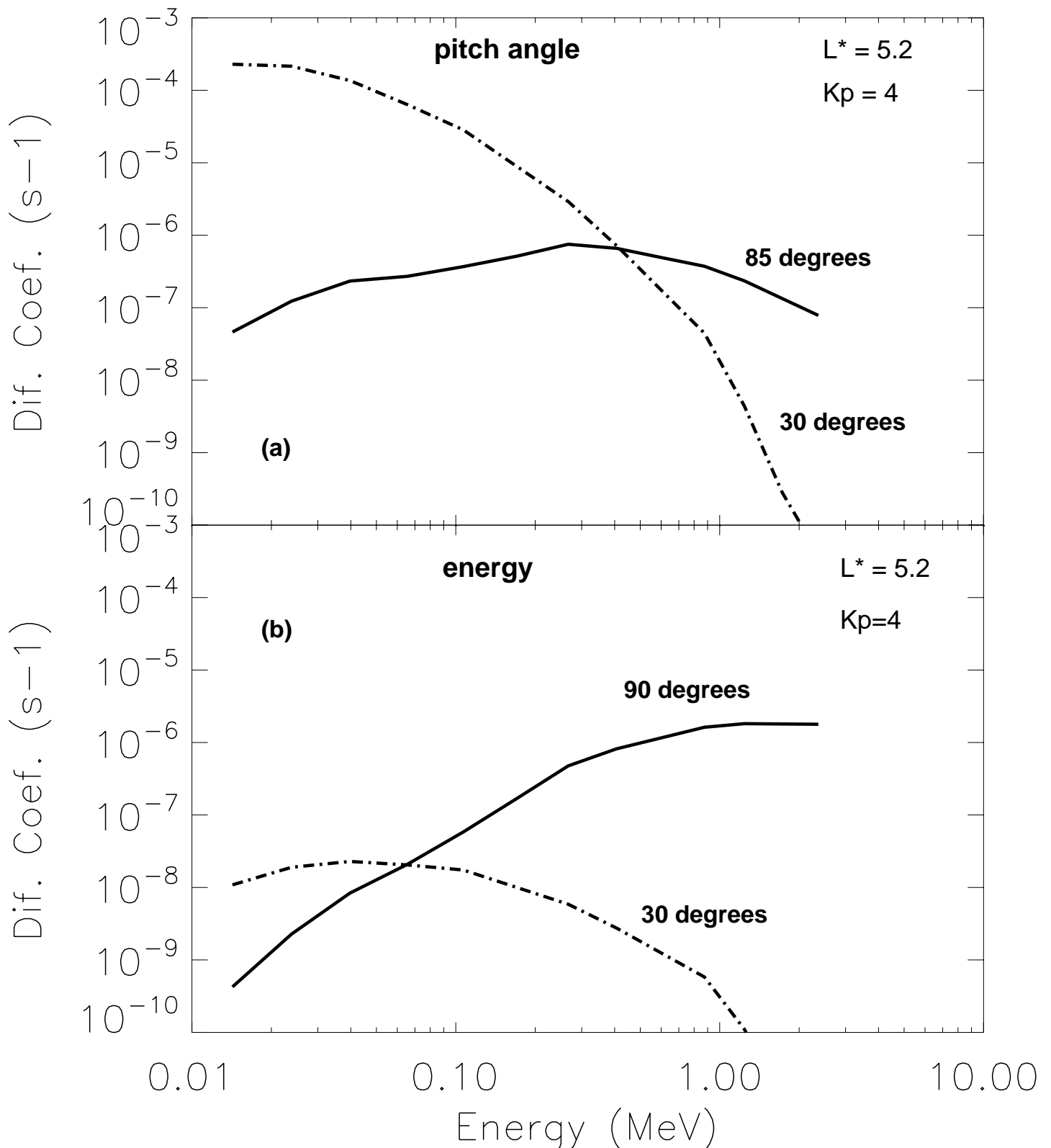
Figure 10. Diffusion coefficients as a function of energy for Kp = 4 and L* = 5.2: (a) pitch angle diffusion coefficients at 90 degrees (solid line) and 30 degrees (dash dot line) and (b) energy diffusion coefficients at 90 degrees (solid line) and 30 degrees (dash dot line).
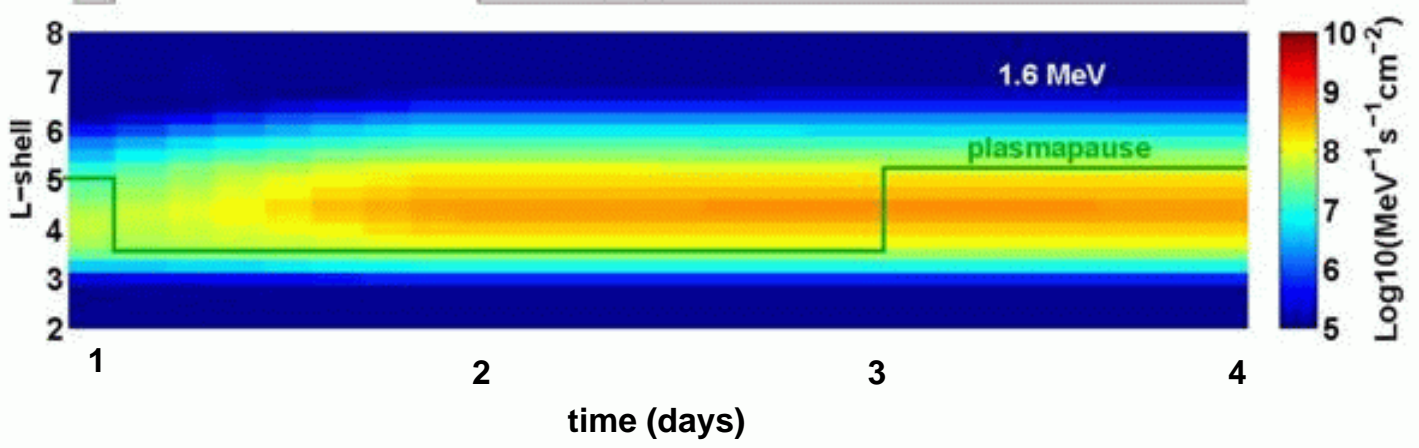
Figure 11. Omnidirectional equatorial flux variation during the test–case simulation for 1.6 MeV electrons. The plasmapause position is marked with a green line.
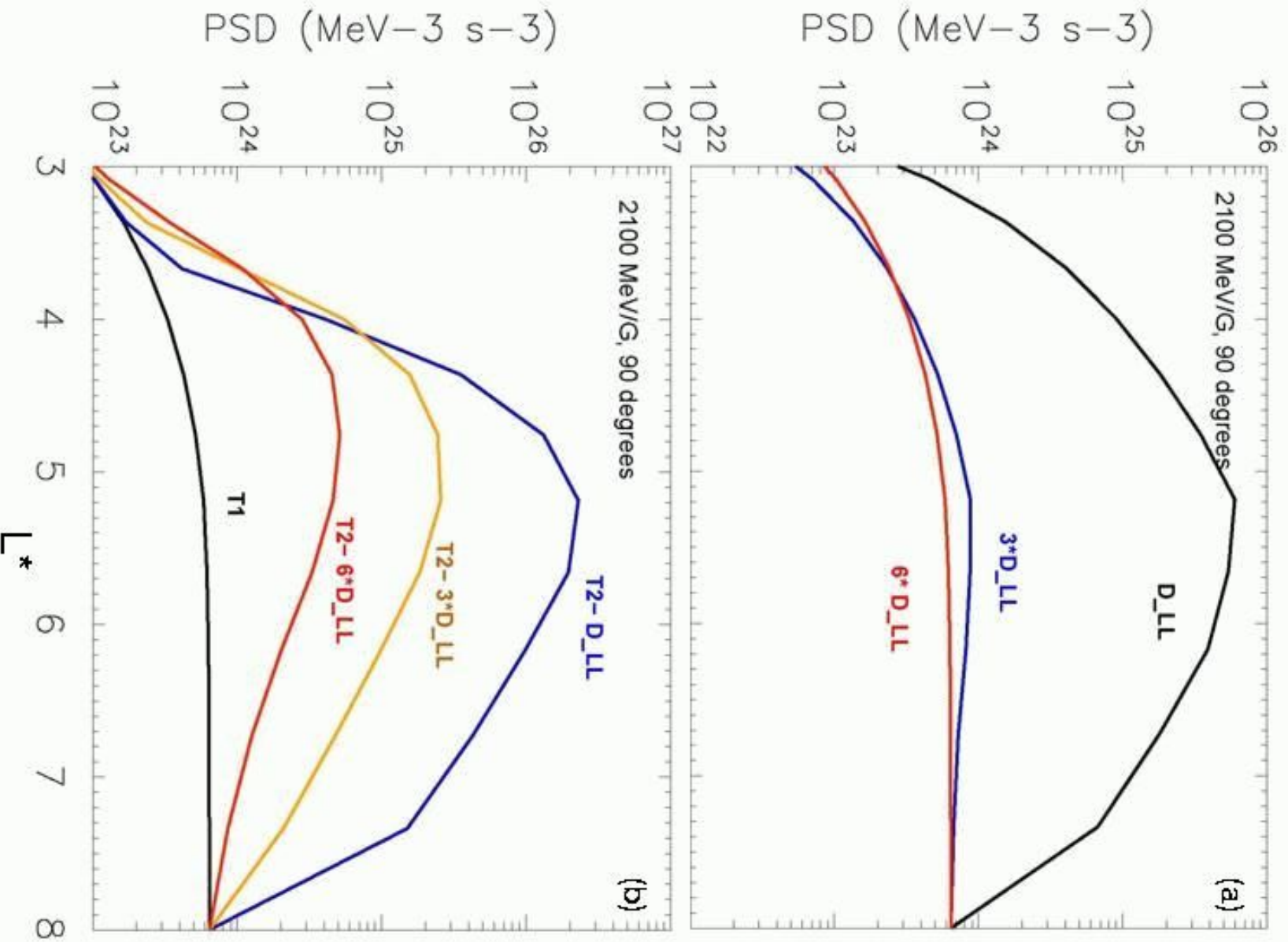
Figure 12. Phase space densities (in $MeV^{-3}s^{-3}$) for 2100 MeV/G equatorial particles as a function of $L*$ for (a) the three steady state simulations and (b) at time T2 for the three dynamic simulations starting from the same initial state at T1.
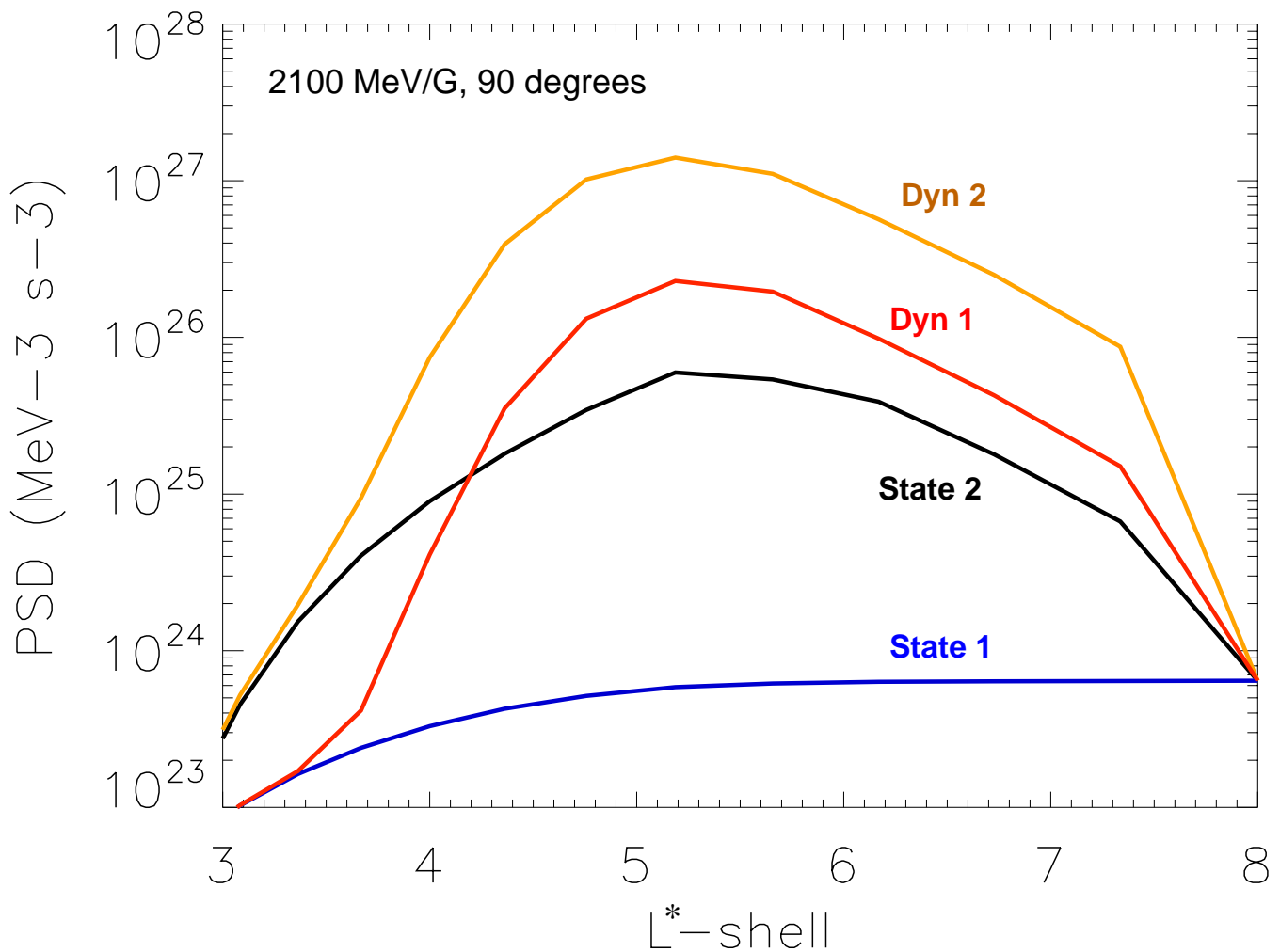
Figure 13. Phase space densities for 2100 meV/G equatorial particles as a function of L* at times T1 and T2 from two dynamic simulations: one starting from State 1 and one starting from State 2.
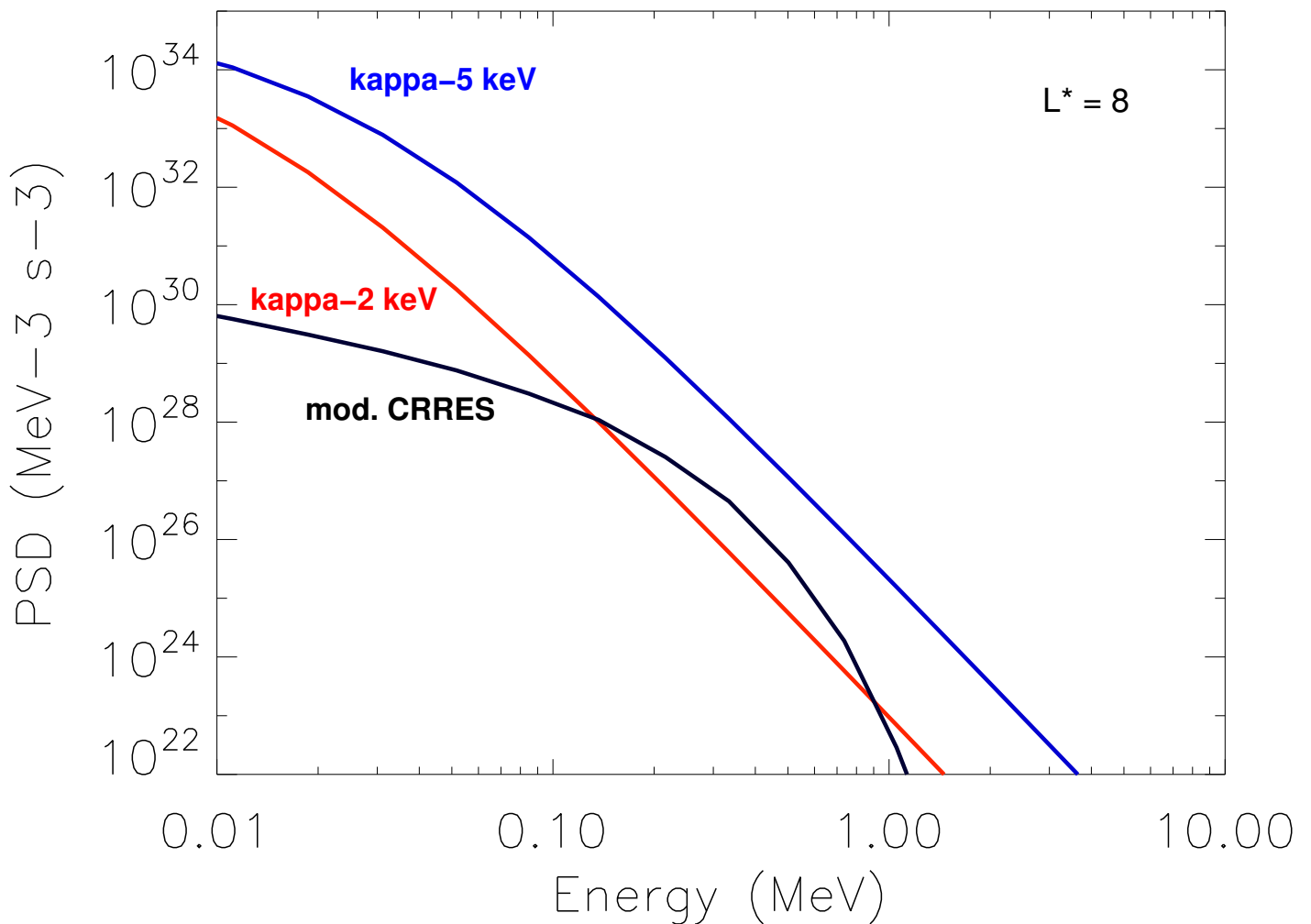
Figure 14. Spectrum of the three distributions used as a source at the outer boundary (L* = 8): the kappa distribution with Eo = 2 keV (red), the kappa distribution with Eo = 5 keV (blue) and the distribution taken from CRRES (black).
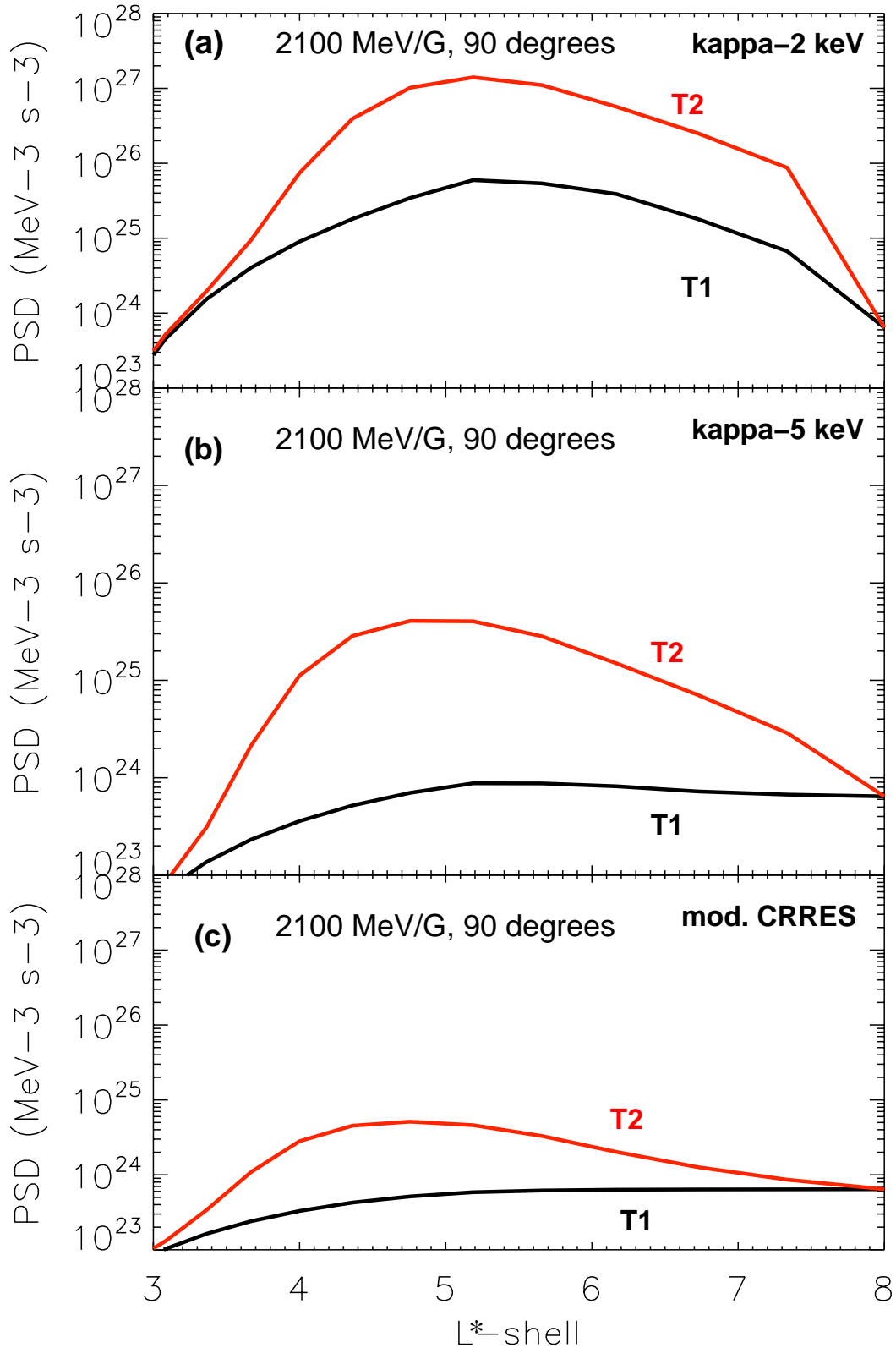
Figure 15. Phase space densities for 2100 MeV/G equatorial particles as a function of L* at times T1 and T2 using the three boundary conditions (a) a kappa distribution with Eo = 2 keV, (b) the kappa distribution with Eo = 5 keV and (c) the distribution taken from CRRES.